Revealing crustal deformation and strain rate in Taiwan using InSAR and GNSS

Kathryn R. Franklin[1] and Mong-Han Huang[1]

[1]University of Maryland, College Park

November 23, 2022

Abstract

Interseismic deformation describes the gradual accumulation of crustal strain within the tectonic plate and along the plate boundaries before the sudden release as earthquakes. In this study, we use five years of high spatial and temporal geodetic measurements, including Global Navigation Satellite System (GNSS) and Interferometric Synthetic Aperture Radar (InSAR) to monitor 3-dimension interseismic crustal deformation and horizontal strain rate in Taiwan. We find significant deformation (strain rate $> 8\text{x}10^{-6}$ yr^{-1}) along the plate boundary between the Philippine Sea Plate and the Eurasian plates in east Taiwan. The high strain rate in the southern part of the Western Foothills is distributed along a few major fault systems, which reveals the geometry of the deformation front in west Taiwan. Our results help identify active faults in southwest and north Taiwan that were not identified before. These findings can be insightful in informing future seismic hazard models.

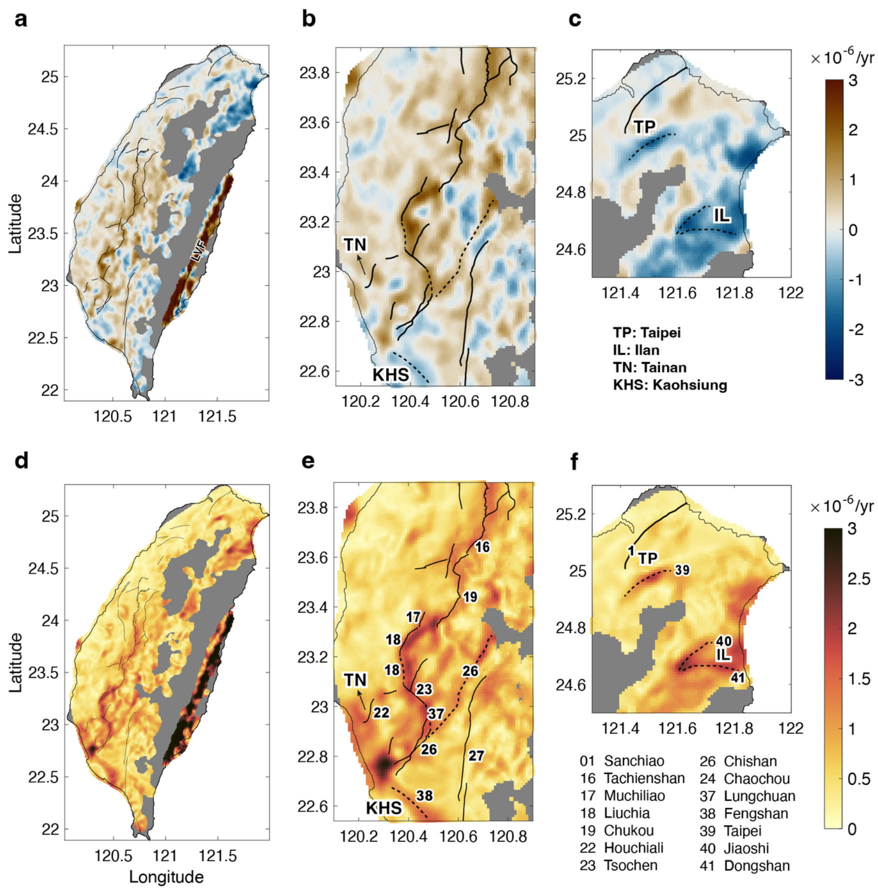
a
b
c
Latitude
Longitude
TP: Taipei
IL: Ilan
TN: Tainan
KHS: Kaohsiung
$\times 10^{-6}$/yr
d
e
f
01 Sanchiao
16 Tachienshan
17 Muchiliao
18 Liuchia
19 Chukou
22 Houchiali
23 Tsochen
26 Chishan
24 Chaochou
37 Lungchuan
38 Fengshan
39 Taipei
40 Jiaoshi
41 Dongshan

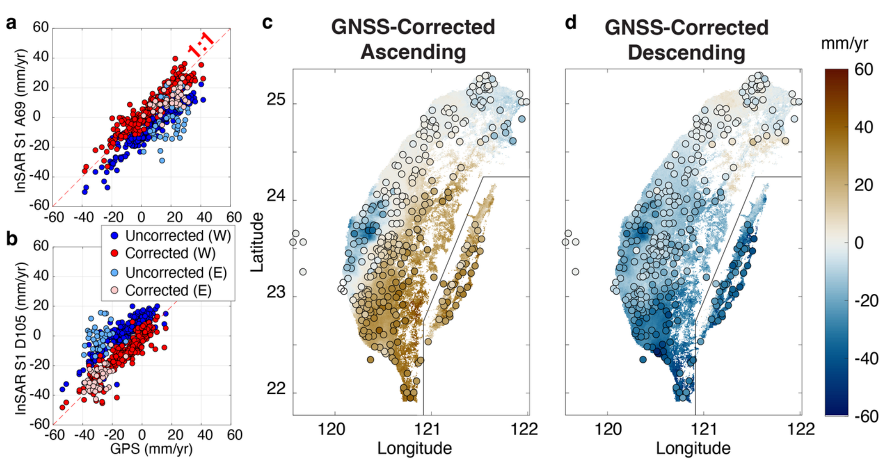
a
b
c
d
InSAR S1 A69 (mm/yr)
InSAR S1 D105 (mm/yr)
GPS (mm/yr)
1:1
Uncorrected (W)
Corrected (W)
Uncorrected (E)
Corrected (E)
GNSS-Corrected Ascending
GNSS-Corrected Descending
mm/yr
Latitude
Longitude

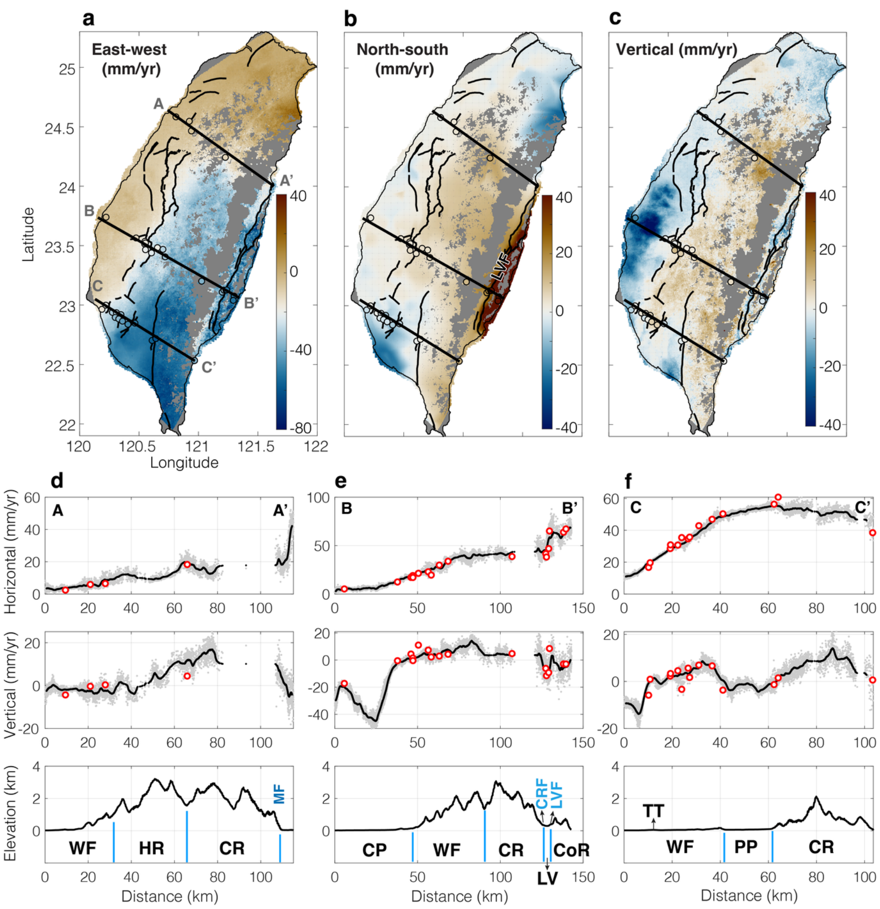
a
East-west (mm/yr)
b
North-south (mm/yr)
c
Vertical (mm/yr)
Latitude
Longitude
A
A'
B
B'
C
C'
LVF
d
e
f
Horizontal (mm/yr)
Vertical (mm/yr)
Elevation (km)
Distance (km)
WF
HR
CR
MF
CP
CRF
LVF
CoR
LV
TT
PP

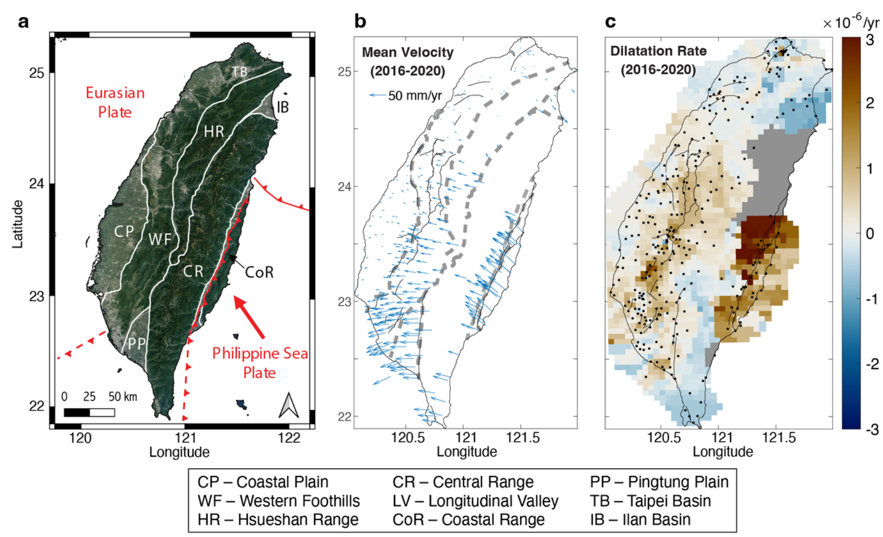
a
Eurasian Plate
Philippine Sea Plate
TB
IB
HR
CP
WF
CR
CoR
PP
0 25 50 km
Latitude
Longitude
b
Mean Velocity (2016-2020)
50 mm/yr
Longitude
c
Dilatation Rate (2016-2020)
$\times 10^{-6}$/yr
Longitude
CP – Coastal Plain
WF – Western Foothills
HR – Hsueshan Range
CR – Central Range
LV – Longitudinal Valley
CoR – Coastal Range
PP – Pingtung Plain
TB – Taipei Basin
IB – Ilan Basin

Revealing crustal deformation and strain rate in Taiwan using InSAR and GNSS

Kathryn R. Franklin and Mong-Han Huang
Department of Geology, University of Maryland, College Park, MD, USA

Abstract

Interseismic deformation describes the gradual accumulation of crustal strain within the tectonic plate and along the plate boundaries before the sudden release as earthquakes. In this study, we use five years of high spatial and temporal geodetic measurements, including Global Navigation Satellite System (GNSS) and Interferometric Synthetic Aperture Radar (InSAR) to monitor 3-dimension interseismic crustal deformation and horizontal strain rate in Taiwan. We find significant deformation (strain rate > 8×10^{-6} yr^{-1}) along the plate boundary between the Philippine Sea Plate and the Eurasian plates in east Taiwan. The high strain rate in the southern part of the Western Foothills is distributed along a few major fault systems, which reveals the geometry of the deformation front in west Taiwan. Our results help identify active faults in southwest and north Taiwan that were not identified before. These findings can be insightful in informing future seismic hazard models.

Plain Language Summary

An earthquake cycle includes three phases: interseismic, coseismic, and postseismic. Interseismic deformation refers to the continuous crustal deformation that is built up by active tectonics. Depending on the relative motion between tectonic plates, the earthquake recurrence interval could vary by a few orders between different locations. As a result, knowing the crustal deformation rate and deformation accumulated in different fault zones can be useful for investigating future earthquake hazards. Using space geodesy tools like Global Navigation Satellite System (GNSS; commonly known as GPS) and Interferometric Synthetic Aperture Radar (InSAR), we can monitor surface deformation during the interseismic period. In this study, we monitor interseismic deformation in Taiwan using geodesy. We find that east Taiwan where two tectonic plates collide has the highest amount of deformation. In southwest and north Taiwan where most of the population resides, there is also high-level of deformation distributed across a few different faults, indicating that some of the faults have a higher risk generating future earthquakes. As a result, knowing the amount of faults slip and deformation built up during this interseismic period may inform us of potential future earthquake hazards.

Key Points

1. This study combines InSAR and GNSS and produces high-resolution 3-D interseismic crustal velocities and strain rate estimates in Taiwan.
2. Strain rate measurements show high surface strain cumulation along east and southwest Taiwan.
3. The surface strain rates and the earthquake hazard models based on seismology and field study-based are in good agreement.

1. Introduction

Taiwan is located between the Eurasian Plate and the Philippine Sea Plate. The Philippine Sea Plate moves towards northwest with a rate of > 80 mm/yr and causes an oblique collision with the Eurasian Plate. This collisional tectonics has given rise to a few geologic provinces, including (from west to east) Chianan Plain (CP), Western Foothills (WF), Hsueshan Range (HR), Central Range (CR), Longitudinal Valley (LV), and the Coastal Range (CoR) (**Figure 1a**). The high collision rate has resulted in a large number of earthquakes in Taiwan, and several devastating events have been located in west Taiwan where the majority of the population resides.

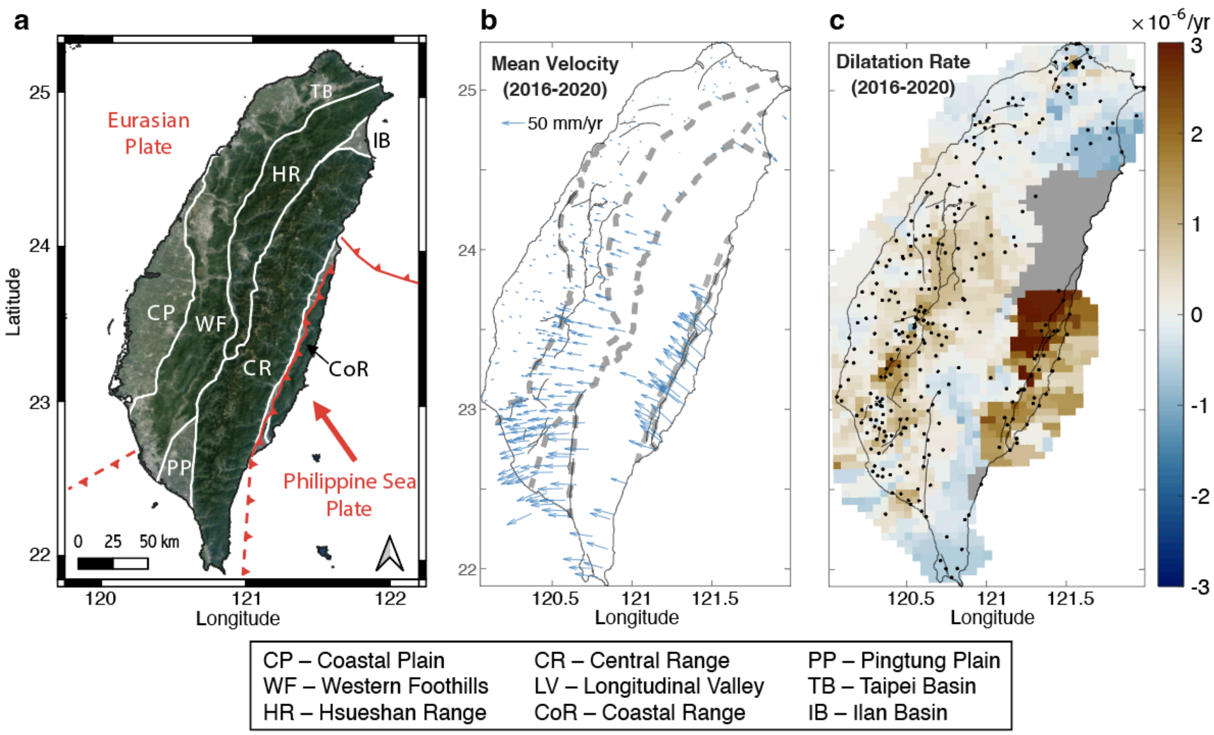

Figure 1. Tectonic setting and crustal deformation of Taiwan. (a) The solid and dashed red lines indicate plate boundaries. The white lines indicate geologic province boundaries. The full name of each geologic province and location is shown below the figure. (b) Mean interseismic GNSS velocities between 2016 and 2021. The black lines are active faults identified by CGS (2021). (c) Dilatation rate based on GNSS data in (b). Black dots are GNSS stations used for the analysis. Gray color represents areas without strain rate results due to lower GNSS network density. Red and blue represent contraction and extension rate (in 10^{-6} yr^{-1}), respectively.

Interseismic deformation describes the gradual accumulation of crustal strain within the tectonic plate and along the plate boundaries before its sudden release as earthquakes. Global Navigation Satellite Systems (GNSS) and Interferometric Synthetic Aperture Radar (InSAR) have been widely used to quantify the interseismic crustal deformation, and interseismic strain accumulation estimated from geodetic measurements can help evaluate potential seismic hazards (Avouac, 2015). Using campaign and continuous GNSS measurements, Yu et al. (1997) and Lin et al. (2010) observed > 80 mm/yr of convergent rate between east Taiwan and the Penghu Islands on the stable continental margin that is ~35 km west of Taiwan (white circles in **Figure 2c**). GNSS measurements also indicate a clockwise rotation in northeast Taiwan that indicates a post-rift opening of the Okinawa Trough as well as lateral extrusion in southwest Taiwan (**Figure 1b**).

Although Taiwan has one of the highest GNSS network densities in the world, GNSS measurements alone still could not confidently identify interseismically creeping faults or deformation associated with closely spaced faults. For example, a GNSS-based dilatation rate map (**Figure 1c**) highlights regions undergoing interseismic contraction in east and southwest Taiwan and extension in northeast Taiwan in a broader scale, but it remains challenging to identify active faults or to determine interseismic fault locking depth of each fault system without high spatial resolution data. Alternatively, InSAR provides high spatial resolution measurements of surface deformation at a cm-level accuracy level (Bürgmann et al., 2000; Elliott et al., 2016). Recent work (e.g., Tong et al., 2012; Shen and Liu, 2020; Weiss et al., 2020) combines GNSS and InSAR to achieve a high spatial resolution with relatively high accuracy. This method is done by utilizing GNSS for the long-wavelength spatial deformation and InSAR for short-wavelength features. Huang and Evans (2019) estimated crustal deformation in southwest Taiwan using 6 years of InSAR-GNSS combined data and were able to characterize fault slip and locking depth of the major fault system using a total variation regularization approach for southwest Taiwan.

In this study, we employ ~5 years of GNSS and InSAR data to generate 3-D interseismic velocities in Taiwan based on data collected between 2016 and 2021. In application, we highlight surface deformation patterns using high resolution 3-D velocities and produce a horizontal strain rate analysis to identify interseismically active faults that can help produce better future seismic hazard models.

2. Data and Method

2.1 SAR and GNSS data collection

The SAR data was obtained from the European Space Agency's (ESA) Sentinel-1 mission for the Copernicus initiative. This mission collects C-band synthetic aperture radar (SAR) acquisitions with a wavelength of 56.7mm and provides single-look complex (SLC) products. In this study, we used Sentinel-1 SAR acquisitions from ascending track 69 and descending track 105 between November 2016 to July 2021. We do not include SAR data before November 2016 to avoid coseismic and to reduce early postseismic deformation of the 2016 M_W 6.4 MeiNong earthquake in southwest Taiwan (e.g. Huang, Tung, et al., 2016). However, our observation period includes the 2018 M_W 6.4 Hualien earthquake in northeast Taiwan (Huang and Huang, 2018). This is because there are sufficient amount of InSAR acquisitions before the Hualien earthquake and the epicenter is offshore. We estimate the coseismic and postseismic components of the Hualien earthquake from the time series analysis (**Supporting Information S1**).

The digital elevation models (DEM) were downloaded from NASA Jet Propulsion Lab's Shuttle Radar Topography Mission (SRTM) with 30m resolution and 3-arc second (Farr et al., 2007), which is stored in the USGS Measures project. The DEM data were used to remove elevation contributions to phase in InSAR images. The weather model used in the troposphere noise correction was downloaded from ECMWF (European Centre for Medium-Range Weather Forecasts) ERA5 weather model products.

The continuous GNSS time series data are processed and maintained by the Central Geologic Survey (CGS), the Central Weather Bureau, the Ministry of Interior, Taiwan, and the

GPS Laboratory at the Institute of Earth Science, Academia Sinica, Taiwan. This data is accessed from Academia Sinica, Taiwan. Additionally, each GNSS station time series was adjusted to remove network adjustment. Similar to the InSAR observation time period, we do not include the GNSS time series before November 2016 in order to reduce contribution from the 2016 MeiNong earthquake. As for the 2018 Hualien earthquake, we do not include GNSS stations within 50 km from the earthquake epicenter in the GNSS analysis.

2.2 InSAR time series processing

The InSAR products were processed using InSAR Scientific Computing Environment (ISCE) software developed at NASA JPL Caltech (Rosen et al., 2012). The TOPS Stack Processor is a module of the ISCE software package that enables SAR images to be combined to generate InSAR images (Fattahi et al., 2017), including applying phase unwrapping using Snaphu (Chen and Zebker, 2002). We used the Stack Sentinel module to generate SAR acquisition pairs by taking orbital data, DEM data, bounding box, auxiliary data (Sentinel-1 instrument parameters), the number of adjacent synthetic aperture radar (SAR) images to be processed and the start and end dates into account. Here we take a network of 3 of adjacent SAR acquisitions in the stack processing.

We used the *Miami InSAR Time Series Software in Python* (Mintpy) (Yunjun et al., 2019) to generate InSAR time series. Mintpy applies tropospheric noise corrections using the ECMWF weather model and generates the time series. We then estimate mean LOS velocities based on the ascending and descending InSAR time series. Mintpy uses a small baseline subsets approach to find the best fitting time series for the given interferograms while minimizing the implied

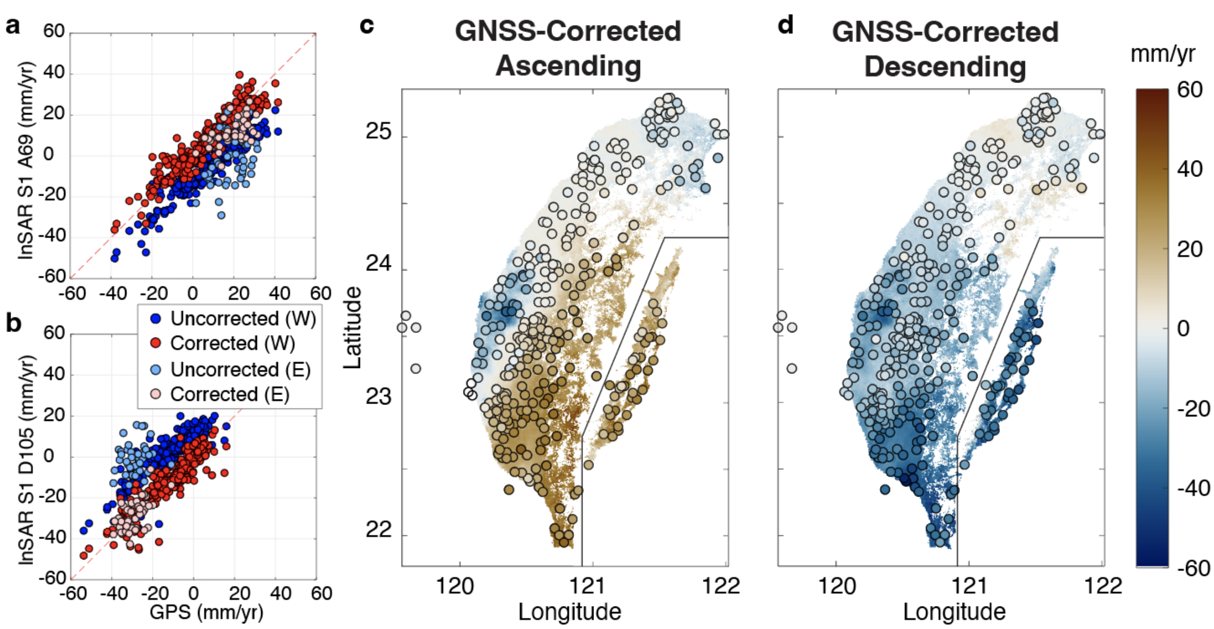

Figure 2. Comparison of InSAR and GNSS velocities. Comparison of velocities before and after correction for ascending (a) and descending (b) tracks. The red dash line in (a) and (b) represents a 1:1 ratio between GNSS and InSAR. W and E in (a) and (b) represent west and east Taiwan, respectively. Positive and negative values in (c) and (d) represent movement towards and award from the satellite LOS, respectively.

velocities (Bernardino et al., 2002). To avoid phase unwrapping errors due to steep mountain ranges and dense vegetation in the Central Range (CR in **Figure 1a**) that could generate a phase offset between west and east Taiwan, we separate the island into west and east Taiwan and perform phase unwrapping separately. Since each part has its own reference point, we merge InSAR results in east and west Taiwan onto a GNSS reference frame.

2.3 Generation of 3-D velocities

Here we briefly document the process of retrieving mean velocities from InSAR and GNSS time series. Details regarding merging InSAR datasets between west and east Taiwan and performing a joint inversion of InSAR and GNSS to estimate 3-D velocities can be found in **Supplementary Information S1**. This process estimates mean velocities from the ascending and descending LOS time series using a polynomial function fit for each InSAR pixel and GNSS station (**Figure S1** as an example). To adjust InSAR velocities to the GNSS reference frame, we first calculate GNSS velocities in InSAR ascending and descending LOS from the 3 components (east-west, north-south, and vertical). For each GNSS station, we use InSAR pixels within 500 m distance from the GNSS station to estimate the average InSAR velocity at the GNSS station in order to reduce InSAR phase noise. As shown in **Figure 2a,b**, besides a consistent shift between InSAR and GNSS ascending or descending velocities, InSAR and GNSS results are quite consistent. This is shown by the nearly 1:1 ratio plus an offset between InSAR and GNSS data distribution (blue circles in **Figure 2c**) due to different reference points between GNSS and InSAR. We use a least square approach to fit InSAR into GNSS-simulated LOS (red circles in **Figure 2c**). After this adjustment, we interpolate GNSS velocities to InSAR samplings using *cubic* interpolation in Matlab. Once this is done, we use the equations that relate LOS and 3-D components for both InSAR and GNSS, and calculate 3-D velocity of each InSAR pixel through a least square inversion. We also use the estimated GNSS and InSAR uncertainty as a weighting matrix in the inversion.

3. 3-D interseismic velocities

The 3-D surface deformation results are shown in **Figure 3**, and the associated uncertainties are shown in **Figures S2 and S3**. The uncertainty analysis, including data misfit estimate and InSAR noise structure is described in **Supporting Information S2**. We consider the mean velocity results to be representative of the interseismic crustal velocities in Taiwan since we have removed contribution from major earthquakes (**Section 2.1**). In the horizontal components, the north-south motion is smoother because it is mostly constrained by the interpolated GNSS data, since InSAR has lower sensitivity to north-south motions. There are no estimated velocities along the east side of the Central Range (CR in **Figure 1a**) because of the high topographic relief that decreases the coherence in most interferograms. The 3-D velocities show up to 40 mm/yr southwestward motion in southwest Taiwan. In east Taiwan, there is > 40 mm/yr northwestward motion along the Longitudinal Valley Fault (LVF in **Figure 3b**). There is observable surface subsidence in the north Coastal Range (CoR in **Figure 1a**), whereas there is more than 20 mm/yr of uplift in the south CoR, which is similar to finding by Hsu and Bürgmann (2006). Along the Central Range, there is up to 20 mm/yr uplift. In the Chianan Plain (CP in **Figure 1a**), there is more than 40 mm/yr surface subsidence due to anthropogenic groundwater pumping (Hung et al., 2010, 2011; Tung and Hu, 2012; Huang, Bürgmann et al., 2016). We plot three transects across the major geologic structure of Taiwan to highlight significant deformation across the island.

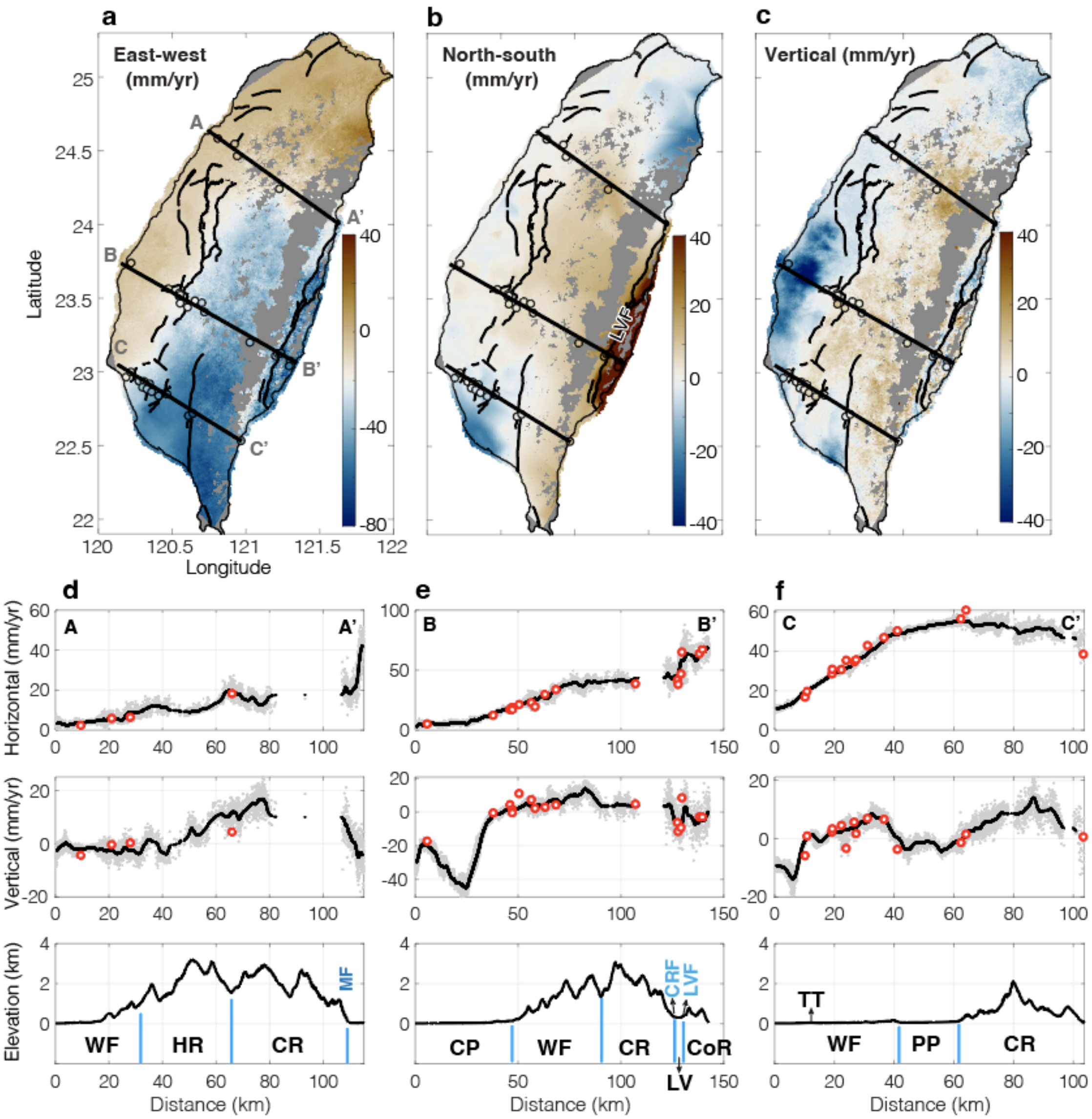

Figure 3. 3-D velocities based on the InSAR-GNSS combined dataset. (a) East-West, (b) North-South, and (c) Vertical velocities. Positive values represent eastward, northward, or upward motions. The black lines are active faults identified by CGS (2021). The colored circles are GNSS stations plotted in the transects. (d), (e), and (f) are three selected transects across the island. In each subplot, the top and middle rows are the horizontal (square root of the east-west and north-south components) and vertical components, respectively. The gray dots are InSAR horizontal or vertical velocities, with the black lines representing the smoothed velocities (smoothing widow size is 100 pixels). The red circles are GNSS mean velocity along the same transect. The bottom of each subplot shows surface topography. The vertical blue lines indicate the geologic boundaries. TT is the location of the Tainan Tableland, and the other abbreviations are the same as those in **Figure 1**.

In transect A (**Figure 3d**), the increase of horizontal motion is not linear, implying change of fault slip rate or locking depth in different geologic units. There is an up to 20 mm/yr increase of horizontal motion across the Milun Fault (MF in **Figure 3d**). However, this motion could be associated with the 2018 Hualien earthquake that significant slip along the Milun Fault (Huang and Huang, 2018), and the postseismic contribution in the InSAR time series may not be entirely removed. The vertical motion is relatively stable in the Western Foothills (WF), followed by a total of 17 mm/yr of uplift in the Hsueshan Range (HR).

Transect B (**Figure 3e**) goes across CP, Western Foothills (WF), CR, and CoR. The horizontal velocity increases by 40 mm/yr from CP to west CR, followed by another rapid increase (20 mm/yr) across LVF. In the vertical component, there is > 40 mm/yr of surface subsidence likely due to anthropogenic activities. The uplift rate gradually increases from WF to CR with a peak uplift rate ~15 mm/yr, which is similar to the long-term uplift rate in Taiwan based on exhumation rate measurements of rocks (Ching et al., 2011). There is ~10 mm/yr of subsidence in the Longitudinal Valley (LV) between CR and CoR. The clear horizontal and vertical velocity offset along LVF suggest shallow fault creep (Lee et al., 2005; Champenois et al., 2012). Although there is a clear vertical offset along the CRF, a lack of horizontal offset across CRF implies the subsidence in LV here could be due to anthropogenic activity. The location of transect B is similar to that presented in both Ching et al. (2011) and Hsu et al. (2018). While the horizontal component is similar to that in Ching et al. (2011), the vertical component is more similar to Hsu et al. (2018).

Transect C (**Figure 3d**) goes across the most active structure of WF. There is ~50 mm/yr of increase in horizontal velocity from west to east WF. The velocity starts to decrease by ~3 cm/yr from west to east CR. In the vertical component, there is subsidence west of the Tainan Tableland (TT in **Figure 3f**), likely related to anthropogenic groundwater pumping. We find clear uplift in WF and CR, but close to no vertical motion in the Pingtung Plain (PP in **Figure 1a**).

4. Strain rate analysis

We calculate the strain rate tensor of Taiwan from the InSAR-GNSS combined dataset. Since surface displacements associated with major earthquakes were removed or estimated in the time series, we consider this dataset representing the interseismic deformation of Taiwan. To reduce computation time, we first downsample the horizontal velocities to 500 m pixel spacing. Since strain rate is differential velocities of pixels divided by pixel distance, it could dramatically amplify short-wavelength noise in InSAR and make the result uninterpretable. For example, 1 mm of noise in 1-D velocity between two pixels 500 m apart can cause longitudinal strain equivalent to 2×10^{-6}. We therefore consider using a group of pixels within a characteristic distance for constructing the strain rate tensor of each grid point. To explore the appropriate length scale of the smoothing, we use a semi-variogram approach suggested by Sudhaus and Jónsson (2009) in a region that is stable in west Taiwan (**Supplementary Information S3)**. We estimate spatially correlated signals in the horizontal velocities and find a characteristic distance of ~7 km (**Figure S6**). Based on this value, when we generate the strain rate tensors we take into account velocities of 144 nearby pixels of each grid point. This number is obtained from the number of pixels that occupy a circular area with 3.4 km radius and 500 m pixel spacing.

The dilatation and the second invariant of the strain rate with 1 km grid spacing are shown in **Figure 4**. In order to reduce the complexity of the fault naming system, we use fault ID numbers consistent with Central Geologic Survey in Taiwan (CGS, 2021) and use the fault ID number than fault names for most of the time hereafter. The fault names are listed below **Figure 4f**. The dilatation rate from the InSAR-GNSS dataset (**Figure 4a**) has much higher spatial resolution than the GNSS-only results (**Figure 1c**). In east Taiwan, the dilatation rate shows a very localized deformation along LVF. In west Taiwan, we find higher contraction rate within WF, along

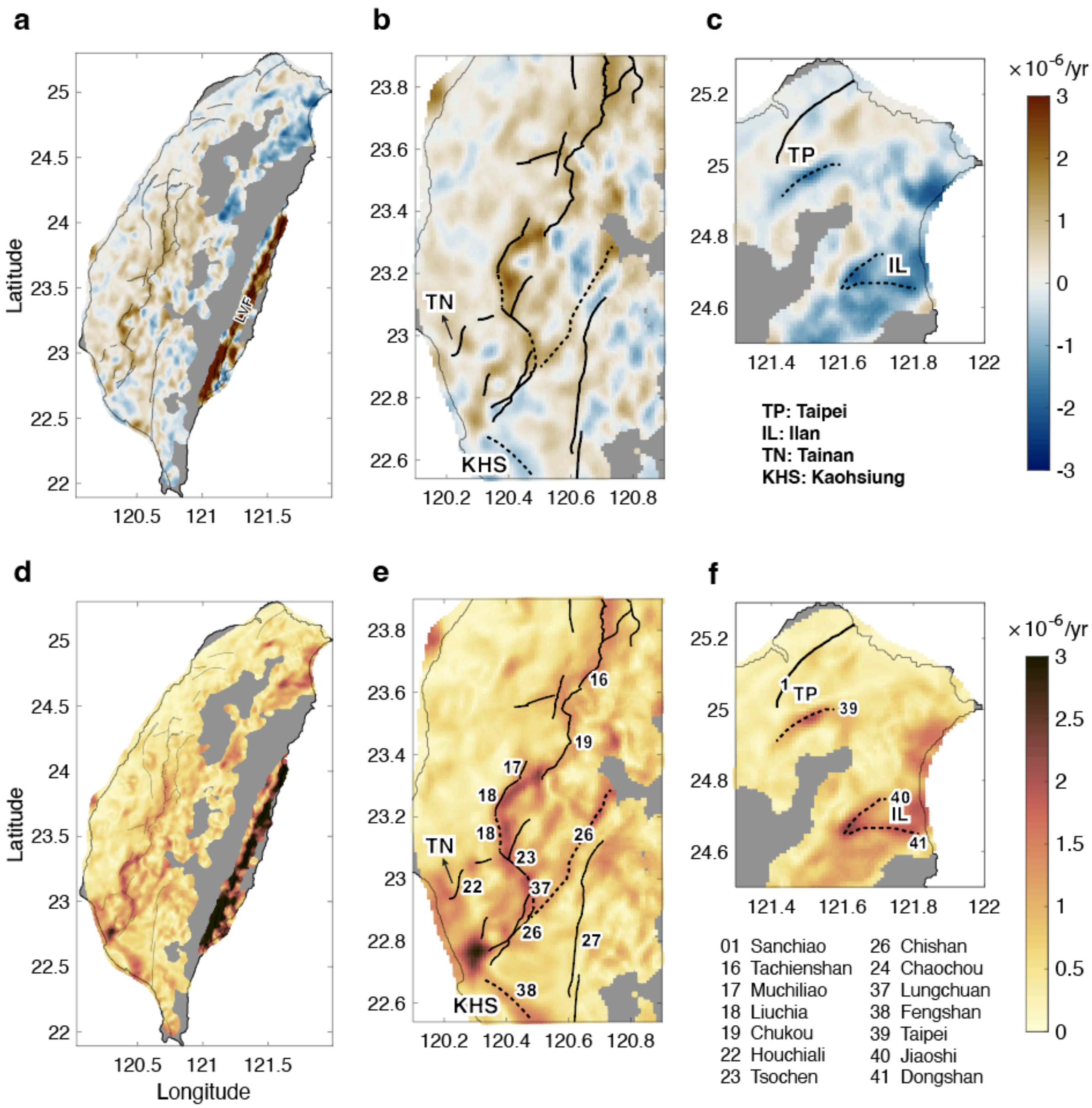

Figure 4. InSAR-GNSS combined strain rate in Taiwan. (a) Dilatation rate. Warm and cold colors indicate contraction and extension, respectively. The color scale is shown in (c). (b) and (c) show the dilatation rate in southwest and north Taiwan, respectively. (d) Second invariant of the strain rate tensor. Warmer color indicates greater amount of deformation. The color scale is shown in (f). (e) and (f) show the second invariant in southwest and north Taiwan, respectively. The black lines in each plot are the active fault traces identified by CGS (2021). In (b) and (c), TN, KHS, TP, and IL are cities (names listed below c). The dashed lines in (b), (c), (e), and (f) are potentially active faults based on strain rate analysis. The numbers in (e) and (f) are faults with names listed below (f). Naming of F37-41 is based on Chen (2016).

several major faults (black fault lines in **Figure 4b**). The distribution of the high second invariant may reveal the deformation front of west Taiwan. In north Taiwan (**Figure 4c**), there is a clear extension along the geologic boundary between CR and HR. We also find a localized extension in the south side of Taipei (TP in **Figure 4c**).

The second invariant of the strain rate tensor (**Figure 4d**) shows the total amount of strain rate (both dilatation and shear). Similar to the dilatation rate, the highest deformation is along LVF with rate > 8×10^{-6} yr^{-1}. Southwest Taiwan has the next highest strain rate after LVF. In a detailed view (**Figure 4e**), there is increased deformation along the major faults (labeled in numbers in **Figure 4e**). This result provides much better spatial resolution of deformation than the GNSS-only products (**Figure 1c**). We additionally find higher strain rate along faults that were not considered active by CGS (2021) but were identified by Chen (2016) based on fieldwork and paleoseismology (indicated by the dashed lines in **Figure 4b,c,e,f)**. In northern Taiwan, in addition to fault ID 39 (or F39), we also find higher deformation in the north and south sides of IL (F40 and F41).

5. Comparing with seismic hazard models

Chan et al. (2020) provided the 2020 version of the Taiwan Earthquake Model (TEM) of Probabilistic Seismic Hazard Analysis (PSHA) following an initial model built by Wang et al. (2016) and fault information by Shyu et al. (2016, 2020). The TEM PSHA model estimates seismic hazard based on a seismogenic structure database, an updated earthquake catalog, time-dependent rupture model, and a revised area source model to estimate the seismic hazard map of Taiwan. With incorporation of Vs30 (shear-wave velocity in the top 30 m depth) for calculating site amplification, the TEM PSHA model identified a few fault structures with an increased seismic hazard potential close to the IB, LV, and southwest WF (see **Figure 1a** for locations). In this section we compare the TEM PSHA model (called *seismic hazard model* hereafter) that predicts future earthquake probability, with the second invariant of the strain rate tensor, which highlights surface strain accumulation over time. Although they do not need to agree, regions with higher interseismic strain accumulation tend to be more seismically active.

We find some similarity between the seismic hazard model and the second invariant of the strain rate tensor. In southwest Taiwan where interseismic strain rate is higher (**Figure 4e**), both F17 and F18 have high seismic potential in the seismic hazard model. However, the distribution of high seismic potential south of F18 is different, where high strain rate diverts into F37 and F22. F22 is in east Tainan Tableland with an estimated ~10 mm/yr creep rate from previous studies (e.g., Huang et al., 2006; Le Béon et al., 2019), but here we additionally find surface deformation west of TN. Further to the southwest side of F26 and along F38, the seismic hazard map does not predict a particularly high seismic probability, whereas high interseismic strain rate is observed. The high strain rate between F22, F26, and F38 could be of concern because Tainan (TN) and Kaohsiung (KHS), the two major cities, are located nearby the fault structures.

In north Taiwan, both the second invariant (**Figure 4f**) and the seismic hazard model show higher deformation and higher seismic probability in Ilan (IL). In Taipei (TP), the capital city of Taiwan, we observed extension strain rate of ~2×10^{-6} yr^{-1} along F39, while the seismic hazard model does not predict a higher hazard potential. F39 (Taipei Fault) has been identified as an inactive reverse fault, but earthquake focal mechanisms near this region show a sign of extension

(Teng et al., 2001). There is also a clear surface subsidence in the TP (**Figure 3c**) as a result of groundwater pumping which is inducing soil compaction, aquifer deformation, and general subsidence (Chen et al., 2007). We cannot discern whether fault creep could have contributed to the surface subsidence near F39. Future studies on seasonal variation of surface movement and how it relates to precipitation and groundwater discharge data may provide further insight into identifying the cause of surface subsidence in this time period.

Again, interseismic surface strain rates do not have to agree with seismic hazard models because they do not inform coseismic displacement. However, a better knowledge of interseismic fault slip, fault locking depth, and detection of active faults may provide significant contributions in advancing fault geometry and slip models for the seismic hazard models. For example, the second invariant result identifies additional faults that are currently active but are not identified as active faults possibly due to limited field mapping or a lack of seismicity during aseismic fault creep, hence not detected using seismology. Future interseismic fault slip models with geodetic constraints can further incorporate fault slip budget (Avouac, 2015). Probabilistic earthquake likelihood models using both geodetic measurements and seismic catalog (e.g., Rollins and Avouac, 2019) may provide insightful contribution to future seismic hazard models.

6. Conclusions

Combining the capabilities of GNSS and InSAR, we can better reveal interseismic crustal deformation of Taiwan. Through a series of GNSS and InSAR comparisons, we find consistency between the two datasets. The InSAR-GNSS combined result shows greater deformation in east and southwest Taiwan, and there is > 40 mm/yr of surface subsidence in west Taiwan due to anthropogenic water pumping and up to 20 mm/yr of uplift in the Central Range. Strain rate analysis suggests > 8×10^{-6} yr^{-1} surface contraction rate along the Longitudinal Valley Fault, and there is also a higher level of contraction in the southwest Western Foothills. The high-resolution strain rate results may reveal the distribution of the deformation front of Taiwan. Our work demonstrates a high spatial resolution of surface deformation that can be revealed by publicly available SAR data with open-source processing tools. Our results highlight creeping faults in east and southwest Taiwan and help identify active faults that were not identified before. These findings can be useful for informing future seismic hazard models.

Acknowledgements

We want to thank Eileen Evans, Chung Huang, Vedran Lekić, and Laurent Montesi for their insightful comments on the original manuscript. MH thanks Kathrine Udell Lopez for proofreading the manuscript. We also thank the GPS laboratory at the Academia Sinica in Taiwan who actively maintains the GNSS stations. This work is supported by NSF EAR 2026099.

Data Sources and Availability Statement

The SLC products containing the SAR images were downloaded from the Alaska Satellite Facility (ASF), University of Alaska database. The precise orbital data of the Sentinel-1 satellites were downloaded from ESA Science Hub. The stack process is part of the ISCE InSAR processing software package (Rosen et al., 2012). Mintpy is an open-source InSAR time series processing software (Yunjin et al., 2019). The InSAR-GNSS dataset and the strain rate results can be found in the Supplementary Datasets. It will also be archived in Zenodo after the peer review process.

References

Avouac, J.-P. (2015). From geodetic imaging of seismic and aseismic fault slip to dynamic modeling of the seismic cycle. Annual Review of Earth and Planetary Sciences, 43(1), 233–271. https://doi.org/10.1146/annurev-earth-060614-105302

Bernardino, P., Fornaro, G., Lanari, R., and Sansosti, E. (2002), Monitoring based on small baseline differential SAR interferograms, *IEEE Transactions on Geoscience and Remote Sensing*, 40, 2375-2383.

Bürgmann, R., Rosen, P. A., & Fielding, E. J. (2000). Synthetic Aperture Radar Interferometry to Measure Earth's Surface Topography and Its Deformation. *Annual Review of Earth and Planetary Sciences, 28*(1), 169-209. doi:10.1146/annurev.earth.28.1.169.

Central Geological Survey (CGS), MOEA (2021). Active fault map of Taiwan. Retrieved from https://faultnew.moeacgs.gov.tw/ckfinder/connector?command=Proxy&type=Attach&currentFolder=/&fileName=2021%20Taiwan%20Fault%20Distribution%20Map%28English%20Version%29.jpg&c=2&p=tblAbout_1&l=4

Champenois, J., Fruneau, B., Pathier, E., Deffontaines, B., Lin, K.-C., and Hu, J.-C. (2012). Monitoring of active tectonic deformations in the Longitudinal Valley (Eastern Taiwan) using Persistent Scatterer InSAR method with ALOS PALSAR data. *Earth and Planetary Science Letters*, *337-338*, 144-155. http://dx.doi.org/10.1016/j.epsl.2012.05.025

Chan, C.-H., Ma, K.-F., Shyu, J. B. H., Lee, Y.-T., Wang, Y.-J., Gao, J.-C., Yen, Y.- T., & Rau, R.-J. (2020). Probabilistic seismic hazard assessment for Taiwan: TEM PSHA2020. *Earthquake Spectra, 36*, 137–159. https://doi.org/10.1177/8755293020951587

Chen, C. W., & Zebker, H. A. (2002). Phase unwrapping for large SAR interferograms: Statistical segmentation and Generalized Network Models. *IEEE Transactions on Geoscience and Remote Sensing*, *40*(8), 1709–1719. https://doi.org/10.1109/tgrs.2002.802453

Chen, C.-T., Hu, J.-C., Lu, C.-Y., Lee, J.-C., & Chan, Y.-C. (2007). Thirty-year land elevation change from subsidence to uplift following the termination of groundwater pumping and its geological implications in the metropolitan taipei basin, Northern Taiwan. *Engineering Geology*, *95*(1-2), 30–47. https://doi.org/10.1016/j.enggeo.2007.09.001

Chen, W.-S. (2016), Introduction to Taiwan geology (in Chinese), published by *Geological Society Located in Taipei*. 250 pp.

Ching, K.-E., Hsieh, M.-L., Johnson, K. M., Chen, K.-H., Rau, R.-J., and Yang, M. (2011), Modern vertical deformation rates and mountain building in Taiwan from precise leveling and continuous GPS observations, 2000–2008, *J. Geophys. Res.*, 116, B08406, doi:10.1029/2011JB008242.

Elliott, J. R., Walters, R. J., and Wright, T. J., (2016), The role of space-based observation in understanding and responding to active tectonics and earthquakes, *Nat. Commun.*, *7*, 13844, doi:10.1038/ncomms13844.

Farr, T. G., et al. (2007), The shuttle radar topography mission, Rev. Geophys., 45, RG2004, doi:10.1029/2005RG000183.

Fattahi, H., Agram, P., & Simons, M. (2017). A Network-Based Enhanced Spectral Diversity Approach for TOPS Time-Series Analysis. *IEEE Transactions on Geoscience and Remote Sensing, 55*(2)*,* 777-786. doi:10.1109/tgrs.2016.2614925

Hsu, L., and Bürgmann, R. (2006), Surface creep along the Longitudinal Valley fault, Taiwan from InSAR measurements, *Geophys. Res. Lett.*, 33, L06312, doi:10.1029/2005GL024624.

Hsu, Y.-J., Lai, Y.-R., You, R.-J., Chen, H.-Y., Teng, L. S., Tsai, Y.-C., et al. (2018). Detecting rock uplift across southern Taiwan mountain belt by integrated GPS and leveling data. *Tectonophysics*, *744*, 275–284. https://doi.org/10.1016/j.tecto.2018.07.012

Huang, M.-H., Hu, J.-C., Hsieh, C.-S., Ching, K.-E., Rau, R.-J., Pathier, E., et al. (2006). A growing structure near the deformation front in SW Taiwan as deduced from SAR interferometry and geodetic observation. *Geophysical Research Letters*, *33*, L12305. https://doi.org/ 10.1029/2005GL025613

Huang, M.-H., Bürgmann, R., & Hu, J.-C. (2016). Fifteen years of surface deformation in southwestern Taiwan: Insight from SAR inter- ferometry. *Tectonophysics*, *692*, 252–264. https://doi.org/10.1016/j.tecto.2016.02.021

Huang, M.-H., Tung, H., Fielding, E. J., Huang, H.-H., Liang, C., Huang, C., & Hu, J.-C. (2016). Multiple fault slip triggered above the 2016 *Mw* 6.4 MeiNong earthquake in Taiwan. *Geophysical Research Letters*, *43*, 7459–7467. https://doi.org/10.1002/2016GL069351

Huang, M.-H., & Huang, H.-H. (2018). The complexity of the 2018 M_w 6.4 Hualien earthquake in east Taiwan. *Geophysical Research Letters*, 45, 13,249– 13,257. https://doi.org/10.1029/2018GL080821

Huang, M.-H., & Evans, E. L. (2019). Total variation regularization of geodetically constrained block models in Southwest Taiwan. *Journal of Geophysical Research: Solid Earth*, *124*. https://doi.org/10.1029/2019JB018076

Hung, W.-C., Hwang, C., Chang, C.-P., Yen, J.-Y., Liu, C.-H., & Yang, W.-H., 2010. Monitoring severe aquifer-system compaction and land subsidence in Taiwan using multiple sensors: Yunlin, the southern Choshui River Alluvial Fan. Environ. Earth Sci. 59, 1535–1548.

Hung, W.-C., Hwang, C., Chen, Y.-A., Chang, C.-P., Yen, J.-Y., Hooper, A., & Yang, C.-Y., 2011. Surface deformation from persistent scatterers SAR interferometry and fusion with leveling data: a case study over the Choushui River Alluvial Fan, Taiwan. Remote Sens. Environ. 115, 957–967.

Le Béon, M., Marc, O., Suppe, J., Huang, M.-H., Huang, S.-T., & Chen, W.-S. (2019). Structure and deformation history of the rapidly growing Tainan anticline at the deformation front of the Taiwan mountain belt. *Tectonics*, 38, 3311– 3334. https://doi.org/10.1029/2019TC005510

Lee, J.-C., Angelier, J., Chu, H.-T., Hu, J.-C., Jeng, F.-S., (2005). Monitoring active fault creep as a tool in seismic hazard mitigation. Insights from creepmeter study at Chihshang, Taiwan. C. R. Geosci. 337 (13), 1200–1207.

Lin, K.-C., Hu, J.-C., Ching, K.-E., Angelier, J., Rau, R.-J., Yu, S.-B., et al. (2010). GPS crustal deformation, strain rate, and seismic activity after the 1999 chi-chi earthquake in Taiwan. *Journal of Geophysical Research*, *115*(B7), B07404. https://doi.org/10.1029/2009JB006417

Rollins, C., & Avouac, J.-P. (2019). A geodesy- and seismicity-based local earthquake likelihood model for central Los Angeles. *Geophysical Research Letters*, 46, 3153– 3162. https://doi.org/10.1029/2018GL080868

Rosen, P. A., Gurrola, E., Sacco, G. F., & Zebker, H. (2012), The InSAR scientific computing environment, Proc. EUSAR, Nuremberg, Germany, 730–733.

Shen, Z.-K., & Liu, Z. (2020). Integration of GPS and InSAR data for resolving 3-dimensional crustal deformation. *Earth and Space Science*, 7, e2019EA001036. https://doi.org/10.1029/2019EA001036

Shyu, J. B. H., Chuang, Y. R., Chen, Y. L., Lee, Y. R., & Cheng, C. T. (2016). A New On-Land Seismogenic Structure Source Database from the Taiwan Earthquake Model (TEM) Project for Seismic Hazard Analysis of Taiwan. *Terrestrial, Atmospheric & Oceanic Sciences*, *27*(3).

Shyu, J. B., Yin, Y.-H., Chen, C.-H., Chuang, Y.-I., & Liu, S.-Ch. (2020). Updates to the on-land seismogenic structure source database by the Taiwan Earthquake Model (TEM) project for seismic hazard analysis of Taiwan. *Terrestrial Atmospheric and Oceanic Sciences. 31,* 469-478. 10.3319/TAO.2020.06.08.01.

Sudhaus, H., & Jónsson, S. (2009). Improved source modelling through combined use of Insar and GPS under consideration of correlated data errors: Application to the June 2000 Kleifarvatn earthquake, Iceland. *Geophysical Journal International*, *176*(2), 389–404. https://doi.org/10.1111/j.1365-246x.2008.03989.x

Teng, L. S., Lee, C.-T., Peng, C.-H., Chu, J.-J., and Chen, W.-F. (2001). Origin and geological evolution of the Taipei Basin, northern Taiwan. West. Pac. Earth Sci.s 1, 115-142

Tong, X., Sandwell, D. T., & Smith-Konter, B. (2013). High-resolution interseismic velocity data along the San Andreas Fault from GPS and InSAR. *Journal of Geophysical Research: Solid Earth, 118*(1), 369-389. doi:10.1029/2012jb009442

Tung, H., Hu, J.-C., 2012. Assessments of serious anthropogenic land subsidence in Yunlin County of central Taiwan from 1996 to 1999 by persistent scatterers InSAR. Tectonophysics 578, 126–135.

Wang, Y.-J., Chan, C.-H., Lee, Y.-T., Ma, K.-F., Shyu, J. B. H., Rau, R.-J., & Cheng, C.-T. (2016). Probabilistic seismic hazard assessment for Taiwan. Terrestrial, Atmospheric and Oceanic Sciences, 27(3), 325-. doi:10.3319/TAO.2016.05.03.01(TEM)

Weiss, J. R., Walters, R. J., Morishita, Y., Wright, T. J., Lazecky, M., Wang, H., . . . Parsons, B. (2020). High-Resolution Surface Velocities and Strain for Anatolia from Sentinel-1 InSAR and GNSS Data. *Geophysical Research Letters, 47*(17). doi:10.1029/2020gl087376

Yu, S.-B., Chen, H.-Y., & Kuo, L.-C. (1997). Velocity field of GPS stations in the Taiwan area. *Tectonophysics*, *274*(1- 3), 41–59. https://doi.org/10.1016/S0040-1951(96)00297-1

Yunjun, Z., Fattahi, H., & Amelung, F. (2019). Small baseline InSAR time series analysis: Unwrapping error correction and noise reduction. *Computers and Geosciences*, 133, 104331. https://doi.org/10.1016/j.cageo.2019.104331

References From the Supporting Information

Fagereng, Å., & Biggs, J. (2019). New perspectives on 'geological strain rates' calculated from both naturally deformed and actively deforming rocks. Journal of Structural Geology, 125, 100-110. https://doi.org/10.1016/j.jsg.2018.10.004

Hussain, E., Hooper, A., Wright, T. J., Walters, R. J., & Bekaert, D. P. (2016). Interseismic strain accumulation across the central North Anatolian Fault from iteratively unwrapped InSAR measurements. *Journal of Geophysical Research: Solid Earth, 121(*12). https://doi.org/10.1002/2016JB013108

Pagani, C., Bodin, T., Métois, M., & Lasserre, C. (2021). Bayesian Estimation of Surface Strain Rates From Global Navigation Satellite System Measurements: Application to the Southwestern United States. Journal of Geophysical Research: Solid Earth, 126(6). doi:10.1029/2021jb021905

Watson, A. R., Elliott, J. R., & Walters, R. J. (2022). Interseismic strain accumulation across the main recent fault, SW Iran, from Sentinel-1 Insar Observations. *Journal of Geophysical Research: Solid Earth*, *127*(2). https://doi.org/10.1029/2021jb022674

AGU PUBLICATIONS

Geophysical Research Letters

Supporting Information for

Revealing crustal deformation and strain rate in Taiwan using InSAR and GNSS

Kathryn R. Franklin and Mong-Han Huang

Department of Geology, University of Maryland, College Park, MD, USA

Contents of this file

Texts S1 to S3
Figures S1 to S13

Additional Supporting Information

Dataset S1: 3-D interseismic velocities
Dataset S2: Strain rate products

Introduction

Text S1 describes InSAR time series processing.
Text S2 describes GNSS and InSAR uncertainty assessment.
Text S3 describes the estimation of surface strain rate.
Figure S1 shows examples of GNSS and InSAR time series fittings.
Figure S2 shows RMS misfits of GNSS and InSAR.
Figure S3 shows uncertainty of InSAR-GNSS combined 3-D velocities.
Figure S4 shows RMS misfits for determining the τ value.
Figure S5 shows the variance with pixel distance in a semi-variogram.
Figure S6 shows the downsampled semi-variogram that highlights the characteristic distance.
Figure S7 shows strain rate maps with different level of smoothing.
Figure S8 shows a schematic of maximum and minimum principal strains.
Figure S9 shows an overview of principal strain rates of Taiwan.
Figure S10 shows an overview of principal strain rates of Taiwan.
Figure S11 shows an overview of dilatation rates of Taiwan.
Figure S12 shows an overview of second invariant of the strain rate tensors of Taiwan.
Figure S13 shows an overview of rotation rates of Taiwan.

Supplementary Text S1: Time Series Processing

For a more in-depth data analysis, a module developed by *Huang and Evans* (2019) was used to (i) re-model the time-series for the ascending and descending LOS InSAR velocities using a polynomial and (ii) re-estimate the ascending and descending LOS InSAR mean velocities to include a GNSS correction.

To exclude low-quality pixels from the ascending track and descending track LOS InSAR data, the temporal and spatial coherence thresholds of the mean ascending and descending LOS InSAR velocities were determined through a trial-and-error method of pixel visibility. Temporal coherence refers to the stability of a pixel throughout time – how similar the pixel phase is between acquisitions. The more stable a pixel, the higher the temporal coherence. Deformation reduces the temporal coherence within reason. Spatial coherence refers to the consistency of a pixel's phase to surrounding pixels. Sharp phase changes between neighboring pixels may indicate an error. We used a temporal coherence threshold of 0.3 for west and east Taiwan, and a spatial coherence threshold of 0.4 for west Taiwan and east Taiwan. The average of the temporal and spatial coherence values above the defined thresholds was determined to be the final coherence value. This final value must be above the final predefined mask value of 0.35. Applying this mask excluded all pixels with values lower than the final coherence value.

After the ascending and descending LOS InSAR velocities were masked, (i) the elevation of each pixel for each interferogram was defined using the DEM, (ii) the look angles and heading directions for each interferogram were defined, (iii) the reference image was set to the first acquisition date for both the ascending and descending track interferograms, and (iv) the latitude and longitude data for the bounding box were linked to the module to geolocate each pixel in each interferogram.

The west Taiwan ascending and descending LOS InSAR velocities were assigned a local reference region in the west, and the east Taiwan ascending and descending LOS InSAR velocities were assigned a local reference region in the east. The designated reference regions were at an area without known faults and minimal seasonal surface movement due to hydrologic cycles and human induced land subsidence. Subsequently, the reference regions were considered as stable regions with zero movement. Once the reference region was defined, the mean velocity of each pixel location throughout time was determined.

To fit the time-series of each pixel for ascending and descending LOS InSAR velocities for both west and east Taiwan, we generated a mathematical model with a linear velocity term, annual periodic terms, and semi-annual periodic terms (Equation S1). The terms utilized match the general pattern of interseismic deformation anticipated in Taiwan. For example, the linear velocity term accounted for the overall mean velocity of the pixel, the annual periodic terms took into consideration the wet and dry seasons’ influence on motion, and the semi-annual periodic terms considered sub-tropical precipitation events (e.g., monsoon vs. typhoon events). These terms for a pixel at location (*x,y*) were represented as:

$$LOS(x,y,t_i) = m_1(x,y) + m_2(x,y)t_i + m_3(x,y)\sin(2\pi t_i) + m_4(x,y)\cos(2\pi t_i) + m_5(x,y)\sin(4\pi t_i) + m_6(x,y)\cos(4\pi t_i) + m_7(x,y)H(t_{\mathrm{EQ}}) + m_8(x,y)\,H(t_{\mathrm{EQ}})\ \ln\left[1 + \left(\frac{t_i - t_{\mathrm{EQ}}}{\tau}\right)\right] \quad \text{[S1]}$$

where m_1 is a constant representing a constant adjustment for the time-series, m_2 is the linear trend of the pixel throughout time, m_3 and m_4 are the annual seasonality of the pixel throughout time, m_5 and m_6 are the semiannual seasonality of the pixel throughout time, m_7 is the Hualien earthquake (i.e., a notable earthquake within the timeframe of interest) displacement coefficient, $H(t_{\mathrm{EQ}})$ is the step function to remove the 2018 M_W 6.4 Hualien Earthquake coseismic event, m_8 represents the postseismic period with a relaxation time of τ = 121 days (See **Text S2.1** for determining this value).

Now, assuming ***G*** matrix represents the mathematical model described in Equation S1,

$$\vec{d} = \boldsymbol{G}\vec{m} \quad \text{[S2]}$$

where $\vec{d}$ is the data vector (LOS (*x, y, t*)), ***G*** is the mathematical model that relates the model parameters to the data (right hand side of Equation S1), and $\vec{m}$ is the model vector ($m_1, m_2, m_3, m_4, m_5, m_6, m_7, m_8$). This mathematical model enables the fitting of a time-series at each pixel location throughout time for both the ascending and descending track data for both west and east Taiwan.

We used a least squares inversion to solve for the mathematical model and estimate the coefficient of each term. This solving approach minimizes the sum of squares of the residuals (Equation S3).

$$\vec{m} = (\boldsymbol{G}^{\boldsymbol{T}}\boldsymbol{G})^{-\mathbf{1}}\boldsymbol{G}^{\boldsymbol{T}}\vec{d} \quad \text{[S3]}$$

where $\vec{m}$ is the model vector, ***G*** is the mathematical model, $\boldsymbol{G}^{\boldsymbol{T}}$ is the transpose of the mathematical model, and $\vec{d}$ is the data vector.

Then, using the pre-processed time-series of each GNSS station, we applied a GNSS-correction to the mean velocities of each pixel derived from the calculated time-series. This correction applied the accuracy of GNSS to the high spatial resolution of InSAR. The GNSS-correction only considered the same time period as the InSAR data and was comparable to the LOS InSAR data as the displacements were projected onto the satellite look angle and heading direction.

To apply the GNSS correction to the ascending and descending LOS InSAR velocities, a ramp model that best fit the InSAR and GNSS data velocity differences was constructed. The coefficients of the ramp model were solved for by inversion (Equation S3) with the velocity residuals as data. Removing the ramp from the uncorrected ascending and descending LOS InSAR velocities produced the GNSS-corrected ascending and descending LOS InSAR velocities. Additionally, the ascending and descending ramps for west and east Taiwan could be applied to the time-series for GNSS correction inclusion.

S1.1 Merge Ascending and Descending from East and West Taiwan

To begin merging the ascending and descending LOS InSAR velocities from west and east Taiwan, the low coherence (or low quality) pixels (e.g., pixels capturing water) from each dataset were masked out and set to 0. High coherence pixels were set to 1, and pixels that were high coherence in both datasets were set to 2. During the GNSS correction, west and east Taiwan were assigned the same reference location; therefore, here, they were merged without searching for a common reference region. For accuracy purposes, if there were overlapping real valued pixels from both datasets, the pixels from the east Taiwan dataset were kept while the pixels from the west Taiwan dataset were set to 0. This merged masking process was done for both the ascending and descending LOS InSAR velocities. Once the masks were created, the values of the real-valued pixels were utilized and datasets with ascending LOS InSAR velocities and descending LOS InSAR velocities for all of Taiwan were created.

S1.2 Convert GNSS-Corrected LOS InSAR & GNSS Velocities

GNSS-corrected LOS InSAR velocities and GNSS velocities were utilized to estimate 3-D deformation: east-west, north-south, and vertical components. First, the GNSS velocities were interpolated to InSAR pixels using 2-D cubic interpolation in Matlab. The mesh size matched the pixel location and size of that from InSAR geocoded to the DEM. The inclusion of these velocities enabled a more accurate 3-D velocity field of Taiwan to be constructed as, for example, InSAR has poor sensitivity to north-south velocities and GNSS velocities are less sensitive to atmospheric phase delays.

The GNSS-corrected LOS InSAR velocities and interpolated GNSS velocities were converted to 3-D deformation by relating the heading direction and look angle of the satellites to the velocity data through an inverse problem in the form of Equation S2. The final velocity product was as follows (Equation S4):

$$\begin{bmatrix} LOS_A \\ LOS_D \\ GNSS_E \\ GNSS_N \\ GNSS_Z \end{bmatrix} = \begin{bmatrix} \cos\phi_A \sin\theta_A & \sin\phi_A \sin\theta_A & -\cos\theta_A \\ \cos\phi_D \sin\theta_D & \sin\phi_D \sin\theta_D & -\cos\theta_D \\ 1 & 0 & 0 \\ 0 & 1 & 0 \\ 0 & 0 & 1 \end{bmatrix} \begin{bmatrix} U_E \\ U_N \\ U_Z \end{bmatrix} \quad \text{[S4]}$$

where data vector $\vec{d}$ contains: $LOS_{A,D}$ the LOS velocity for the ascending and descending tracks and $GNSS_{E,N,Z}$ the interpolated GNSS velocities in east, north, and vertical, respectively. Matrix $\boldsymbol{G}$ contains: ϕ_A and ϕ_D the satellite heading direction for the ascending and descending tracks and θ_A and θ_D the satellite look-angle of the ascending and descending tracks, respectively. This matrix relates the InSAR and GNSS velocities to their 3-D components. Model vector $\vec{m}$ contains the 3-D velocity outputs $U_{E,N,Z}$.

The linear inverse problem was solved for using a least squares inversion to minimize the sum of squares of residuals and to determine the best fit model (Equation S3). Additionally, in order to weigh each component of the output 3-D velocity dataset based on misfit, we incorporated a weighting matrix $\boldsymbol{W}$ into the least squares inversion (Equation S5).

$$\vec{m} = (\boldsymbol{G}^{\boldsymbol{T}}\boldsymbol{W}\boldsymbol{G})^{-1}\boldsymbol{G}^{\boldsymbol{T}}\boldsymbol{W}^{\boldsymbol{T}}\vec{d} \quad \text{[S5]}$$

where matrix $\boldsymbol{W}$ (Equation S6) is used to weigh the data and is solved for during **Text S2.1**.

$$\boldsymbol{W} = \begin{bmatrix} \varepsilon_A{}^{-2} & 0 & 0 & 0 & 0 \\ 0 & \varepsilon_D{}^{-2} & 0 & 0 & 0 \\ 0 & 0 & \varepsilon_{GNSS_E}{}^{-2} & 0 & 0 \\ 0 & 0 & 0 & \varepsilon_{GNSS_N}{}^{-2} & 0 \\ 0 & 0 & 0 & 0 & \varepsilon_{GNSS_Z}{}^{-2} \end{bmatrix} \quad [S6]$$

where matrix ***W*** is the weighting matrix and ε for ascending, descending, and GNSS represents the misfit values produced from the inversion of Equation S1.

Using the resulting 3-D velocity outputs, the Final InSAR and GNSS (FIG) dataset was created. This dataset includes: the weighted mean GNSS-corrected InSAR / interpolated GNSS velocity values with the associated uncertainties and the GNSS velocity values with the associated uncertainties. The GNSS velocity values were appended to the dataset for additional data point inclusion. Uncertainties are solved during **Text S2.2**. Additionally, a Reduced FIG dataset was created, which contained the values within the FIG dataset downsampled to every 10 pixels in both the x- and y-direction. The FIG and Reduced FIG datasets contain pixels that are 50 m x 50 m and 500 m x 500 m, respectively.

Supplementary Text S2: Error Analysis

We incorporated an error analysis into the InSAR and GNSS velocity solutions by determining root mean square (RMS) misfit. As previously mentioned, the calculated misfit was used to define the weighting matrix, ***W*** (Equation S6), to properly weigh between the GNSS-corrected InSAR and the interpolated GNSS velocities. The uncertainties, inferred from misfit, produced by taking the LOS and GNSS velocities to east-west, north-south, and vertical were utilized to confirm consistent transformation and were appended to the FIG dataset for later usage. Furthermore, to distinguish tectonic signal from noise in the deformation rate analysis, we quantified distance-correlated noise structure using a semi-variogram and covariogram model for a region without known surface deformation.

S2.1 Solving for RMS Misfit and τ

When constructing the mathematical model (Equation S1) that best fits the velocity data, we calculated the RMS misfit to detail the misfit between the model and the observed velocity values (Equation S8). Specifically, the RMS misfit was calculated for the ascending and descending LOS InSAR data (every pixel in every scene) and the east-west, north-south, and vertical GNSS data (every station in every epoch). Since west and east Taiwan were processed separately, the west and east Taiwan InSAR misfits were calculated separately and then merged.

$$E(x,y) = \sqrt{\frac{1}{N}\sum_{i=1}^{N}\left(\vec{d}_i(x,y) - \vec{m}_i(x,y)\right)^2} \; for\ i = 1, \dots N; \qquad \text{[S8]}$$

where $E(x,y)$ is the RMS misfit of pixel (x,y), $\vec{d}_i$ is observed velocity data, and $\vec{m}_i$ is best fit model velocity data, *i* is the index of an acquisition, and *N* is the total number of acquisitions.

Additionally, to determine the relaxation time (τ) for removing the postseismic contribution from the 2018 $M_W 6.4$ Hualien Earthquake in the mathematical model (Equation S1), we calculated the RMS misfit of all the pixels with a given τ value between 1 and 600 days in a 20-day step size:

$$E(\tau_j) = \sqrt{\frac{1}{N}\sum_{i=1}^{N}(\vec{d}_i(\tau_j) - \vec{m}_i(\tau_j))^2} \; for\ i = 1, \dots N;\ j = 1, \dots 600\ \text{(days)}; \qquad \text{[S9]}$$

where $E(\tau_j)$is the RMS misfit of relaxation time (τ) in *j* days, $\vec{d}_i$ is observed velocity data, and $\vec{m}_i$ is best fit model velocity data, *i* is the index of an acquisition, and *N* is the total number of acquisitions. The relaxation time that produced the least amount of misfit was used in Equation S1.

S2.2 Uncertainty Assessment

The uncertainty of every pixel was solved by evaluating the misfit of the inversion that transformed the LOS InSAR and GNSS velocities to 3-D velocities. The uncertainty values at each time were inferred from the velocity misfit values using a linear inverse problem in the $\vec{d} = \boldsymbol{G}\vec{m}$ form (Equation S10):

$$\begin{bmatrix} \varepsilon_A(x,y) \\ \varepsilon_D(x,y) \\ \varepsilon\ GNSS_E(x,y) \\ \varepsilon\ GNSS_N(x,y) \\ \varepsilon\ GNSS_Z(x,y) \end{bmatrix} = \begin{bmatrix} \cos\phi_A(x,y)\sin\theta_A(x,y) & \sin\phi_A(x,y)\sin\theta_A(x,y) & -\cos\theta_A(x,y) \\ \cos\phi_D(x,y)\sin\theta_D(x,y) & \sin\phi_D(x,y)\sin\theta_D(x,y) & -\cos\theta_D(x,y) \\ 1 & 0 & 0 \\ 0 & 1 & 0 \\ 0 & 0 & 1 \end{bmatrix} \begin{bmatrix} Unc_E(x,y) \\ Unc_N(x,y) \\ Unc_Z(x,y) \end{bmatrix} \quad \text{[S10]}$$

where data vector $\vec{d}$ contains: $\varepsilon_{A,D}\,(x,y)$ the misfit for the ascending and descending track pixels and $\varepsilon\ GNSS_{E,N,Z}\,(x,y)$ the interpolated GNSS misfit for east, north, and vertical, respectively. Matrix $\boldsymbol{G}$ contains: ϕ_A and ϕ_D the satellite heading direction for the ascending and descending tracks and θ_A and θ_D the satellite look-angle of the ascending and descending tracks, respectively. This matrix relates the GNSS-corrected InSAR / interpolated GNSS velocities to their 3-D components. Model vector $\vec{m}$ contains the 3-D velocity uncertainty estimates, $Unc_{E,N,Z}$, for east, north, and vertical components, respectively. The identity matrix is used to bring the GNSS misfit values through the inverse problem with no transformation as they are already in 3-D form.

S2.3 Noise Structure Contributions in the Deformation Rate Analysis

To determine which level of smoothing best eliminated the noise structure contribution, I calculated a semi-variogram model and covariogram model of a non-deforming region for error estimation (*Sudhaus and Jonsson*, 2009). The semi-variogram was modeled from pixel variance with distance in the x- and y-direction (Equation S11) and suggested the use of an exponential equation to model the covariogram (Equation S12). The covariogram estimated pixel spatial correlation with distance (i.e., covariance) (*Sudhaus and Jonsson*, 2009).

The semi-variogram was defined as (Equation S11):

$$S(r) = \sigma^2(1 - e^{-\frac{r}{\lambda}}) \quad \text{[S11]}$$

where $S(r)$ is the modeled semi-variogram between two pixels, σ^2 is the variance, r is the distance between the two pixels, and λ is the characteristic wavelength of the transect.

The modeled covariogram, produced from an exponential mathematical model, was defined as (Equation S12):

$$C(r) = \sigma^2 e^{-\frac{r}{\lambda}} \quad [S12]$$

where $C(r)$ is the covariance between two pixels, σ^2 is the variance, r is the distance between the two pixels, and λ is the characteristic wavelength of the transect.

The modeled semi-variogram was solved for with an exponential, spherical, and gaussian mathematical model. The exponential model fit best and was subsequently utilized to model the covariogram. The unknown σ^2 and λ in the covariogram model (Equation S12) were solved using an inverse problem with the FIG dataset velocities for a non-deforming region as data constraints. The covariogram model acted to estimate the characteristic wavelength of correlation to quantify the assumption that variables closer in distance tend to be more similar (Watson et al., 2022; Hussain et al., 2016). Therefore, a smoothing window size that is smaller than the characteristic distance λ at which pixels were spatially correlated may display noise signals and not accurately capture the tectonic deformation influencing the region. Given that the deformation tensor was calculated every 1 km and each pixel is 500 m x 500 m in the Reduced FIG dataset, utilizing the nearest 30, 144, and 420 pixels resulted in a 1.5, 3.4, and 5.8 km radius of values being incorporated into the tensor, respectively (**Figure S7**).

Supplementary Text S3: Deformation rate analysis

S3.1 Dilatation, Maximum Shear, and 2nd Invariant

The deformation tensor defines position change within a body due to external forces (**Figure S8**). Using the Reduced FIG dataset, I determined the deformation rate tensor every 1 km where the InSAR samples were located every 500 m. The calculated deformation rate tensors considered the nearest 30, 144, and 420 pixels. From this, we calculated dilatation (unit: yr^{-1}), maximum shear (unit: yr^{-1}), and 2nd invariant (unit: yr^{-1}). Note: Dilatation, maximum shear, and 2nd invariant refer to their rate per year. The purpose of the deformation rate analysis was to quantify 2-D deformation fields across Taiwan. This analysis assumed that deformation fields were subject to variations in stress rather than strength (Fagereng and Biggs, 2019).

The deformation rate tensor is defined as:

$$\dot{\boldsymbol{D}} = \begin{bmatrix} \dot{D}_{xx} & \dot{D}_{xy} \\ \dot{D}_{yx} & \dot{D}_{yy} \end{bmatrix}$$

$$= \begin{bmatrix} \dot{D}_{xx} & \frac{1}{2}\,(\dot{D}_{xy} + \dot{D}_{yx}) \\ \frac{1}{2}\,(\dot{D}_{xy} + \dot{D}_{yx}) & \dot{D}_{yy} \end{bmatrix} + \begin{bmatrix} 0 & \frac{1}{2}\,(\dot{D}_{xy} - \dot{D}_{yx}) \\ -\frac{1}{2}\,(\dot{D}_{xy} - \dot{D}_{yx}) & 0 \end{bmatrix}$$

$$= \begin{bmatrix} \frac{\partial V_E}{\partial x} & \frac{1}{2}\,(\frac{\partial V_E}{\partial y} + \frac{\partial V_N}{\partial x}) \\ \frac{1}{2}\,(\frac{\partial V_E}{\partial y} + \frac{\partial V_N}{\partial x}) & \frac{\partial V_N}{\partial y} \end{bmatrix} + \begin{bmatrix} 0 & \frac{1}{2}\,(\frac{\partial V_E}{\partial y} - \frac{\partial V_N}{\partial x}) \\ -\frac{1}{2}\,(\frac{\partial V_E}{\partial y} - \frac{\partial V_N}{\partial x}) & 0 \end{bmatrix} \qquad \text{[S13]}$$

where the deformation rate tensor, $\dot{\boldsymbol{D}}$, is the sum of the strain rate (irrotational) matrix and rotational rate matrix. $\frac{\partial V_E}{\partial x} = \dot{D}_{xx}$, $\frac{\partial V_N}{\partial y} = \dot{D}_{yy}$, and $\frac{1}{2}\,(\frac{\partial V_E}{\partial y} + \frac{\partial V_N}{\partial x}) = \frac{1}{2}\,(\dot{D}_{xy} + \dot{D}_{yx})$. The off-diagonal terms in the rotational matrix are equal in quantity but change in sign.

Using components of the deformation rate tensor, I solved for dilatation, the overall change in volume due to deformation. Dilatation is the sum of principal strains, which are the eigenvalues of a strain rate tensor (Equations S14 & S15).

$$|\,\mathbf{A} - \lambda \cdot \mathbf{I}\,| = 0 \qquad \text{[S14]}$$

where **A** is the strain tensor, λ are the eigenvalues, and **I** is the identity matrix. The | | sign represents the determinant operation.

$$\delta = \varepsilon_1 + \varepsilon_2 \qquad \text{[S16]}$$

where δ is dilatation and ε_1 and ε_2 are the maximum and minimum principal strains (i.e., eigenvalues).

Then, maximum shear was solved to determine the factor in which deformation occurred in a specific direction (Equation S16). In this case, maximum shear (i.e., change in shape/angle) corresponds to the greatest shear at 45° to the principal strains.

$$\gamma_{max} = \frac{\varepsilon_1 - \varepsilon_2}{2} \qquad \text{[S16]}$$

where γ_{max} is maximum shear and ε_1 and ε_2 represent the maximum and minimum principal strains (i.e., eigenvalues).

Invariants of the deformation rate tensor are properties that do not change under coordinate rotation. The 2nd invariant of strain rate determines the total strain rate accumulation of the area of interest, which highlights localities with increased seismic risk (Equation S17) (Pagani et al., 2021). It acts as a combination of both the dilatation (contraction and extension) and maximum shear stress.

$$I_2 = \sqrt{D_{xx}^2 + D_{yy}^2 + 2\left[\frac{1}{2}(D_{xy} + D_{yx})\right]^2} \qquad \text{[S17]}$$

where I_2 is 2nd invariant of strain rate and D_{xx}, D_{yy}, D_{xy}, D_{yx} are components of the symmetric strain rate tensor. D_{xy} and D_{yx} cannot be assumed to be of the same value as rotation, which does not address shape change and is not taken into consideration.

Supplementary Figures

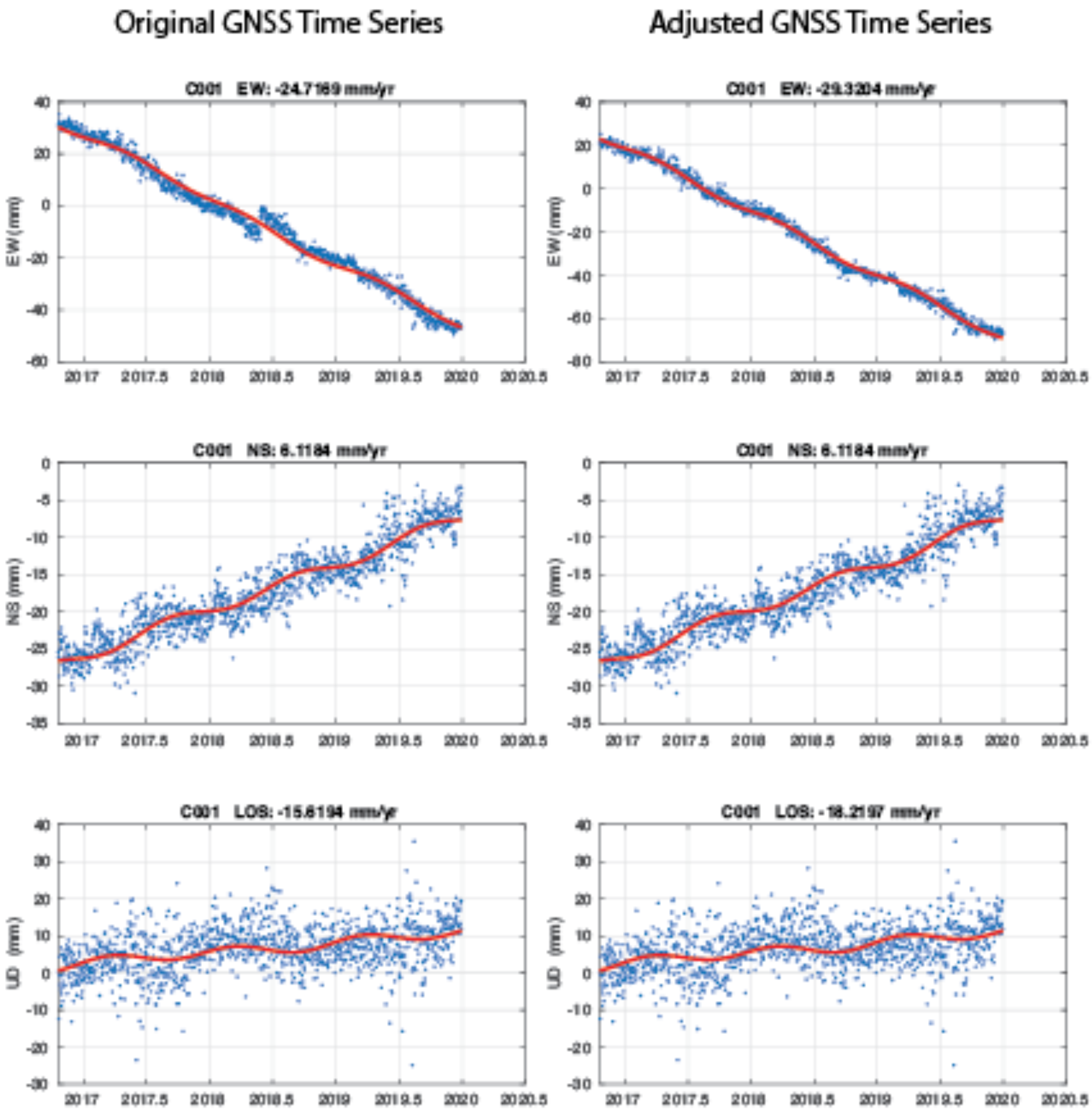

Figure S1. Example of GNSS time-series manual adjustment showing the original time-series of GNSS station C001 in Taiwan (lat/lon: 23.418/120.612) and the adjusted time-series of GNSS station C001. The adjustment is located at 2018.4 in the east-west motion time-series.

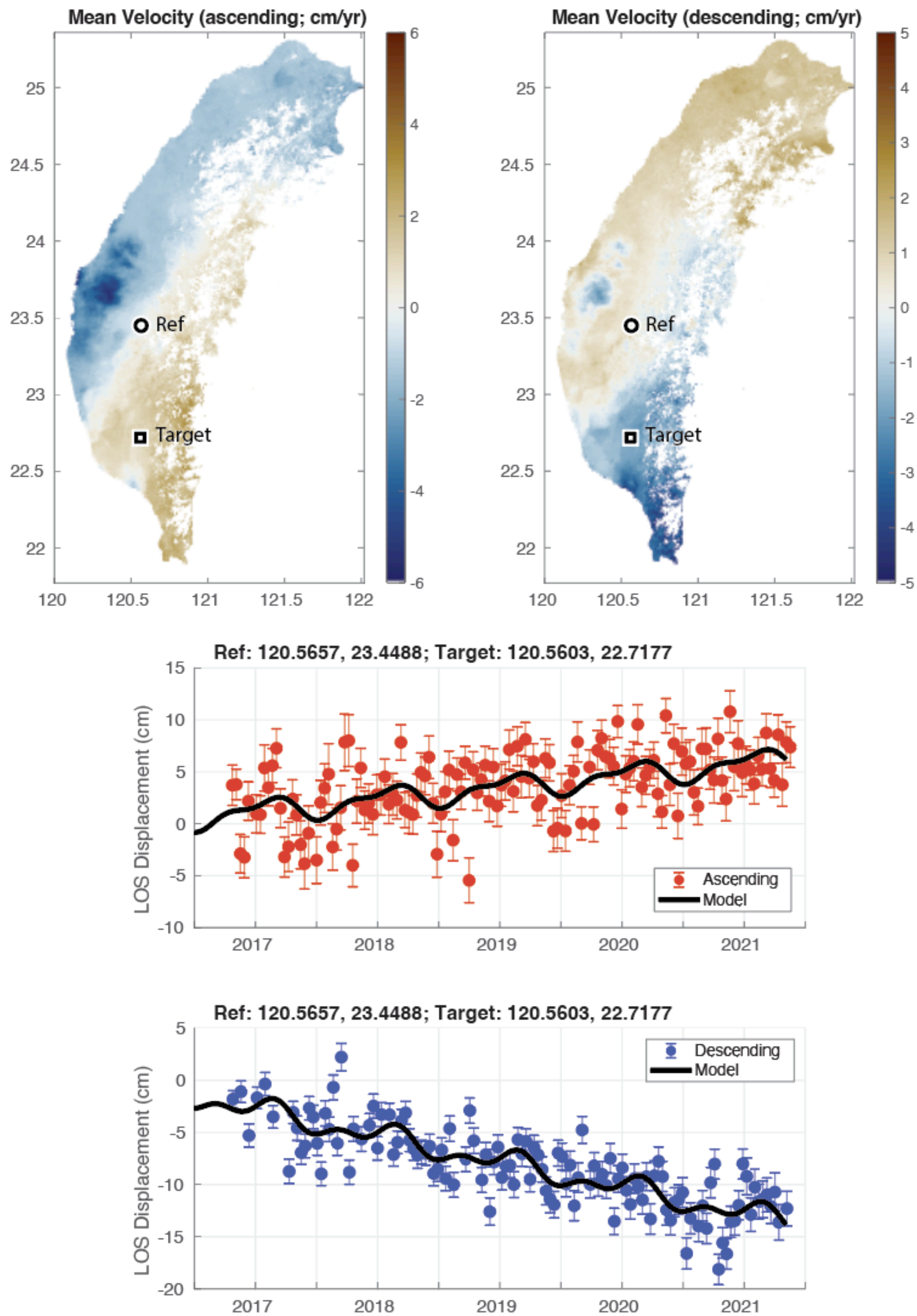

Figure S1 (cont.). Example InSAR time series for west Taiwan. The two maps show mean velocity in ascending and descending tracks. The time series are motions relative to the reference point (lat/lon shown in the title of the time series plot). The back curve is the modeled time series using Equation S1.

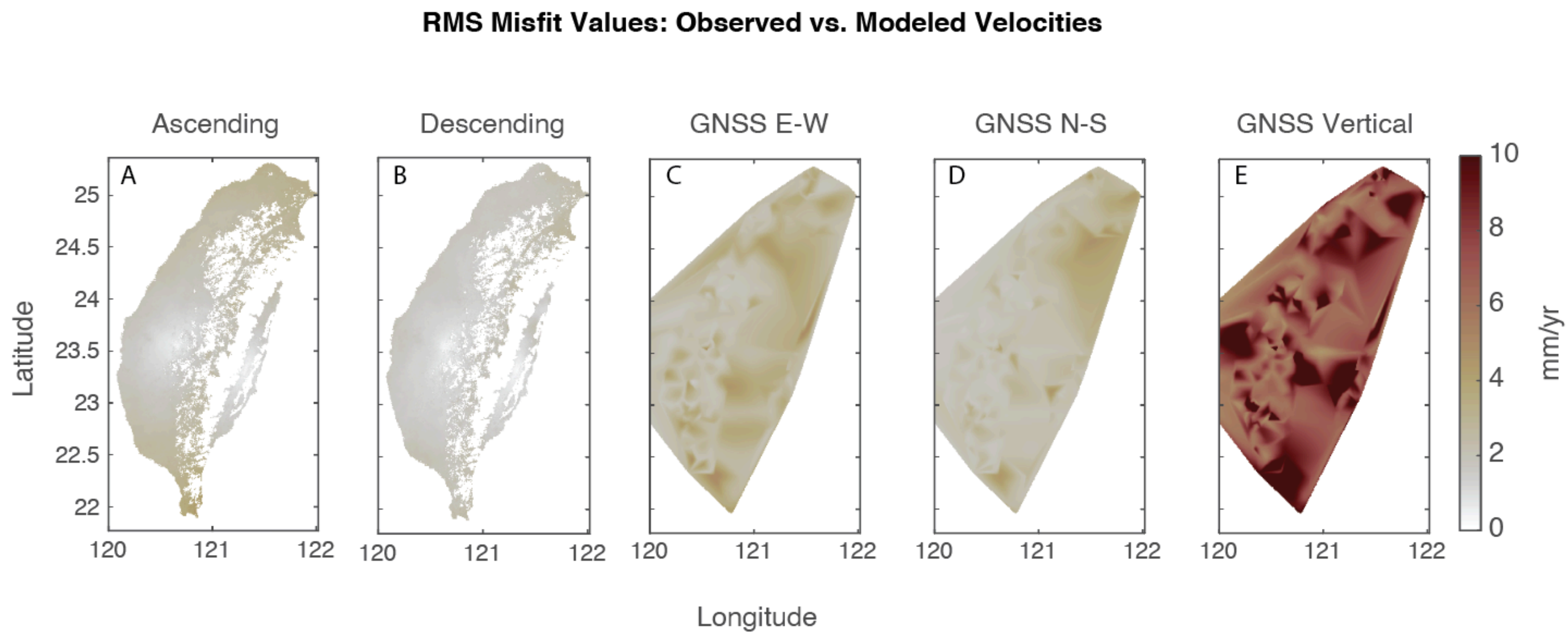

Figure S2. RMS misfits produced from the transformation of observed (A) ascending and (B) descending LOS InSAR velocities and interpolated (C) east-west, (D) north-south, and (E) vertical GNSS velocities to modeled velocity values.

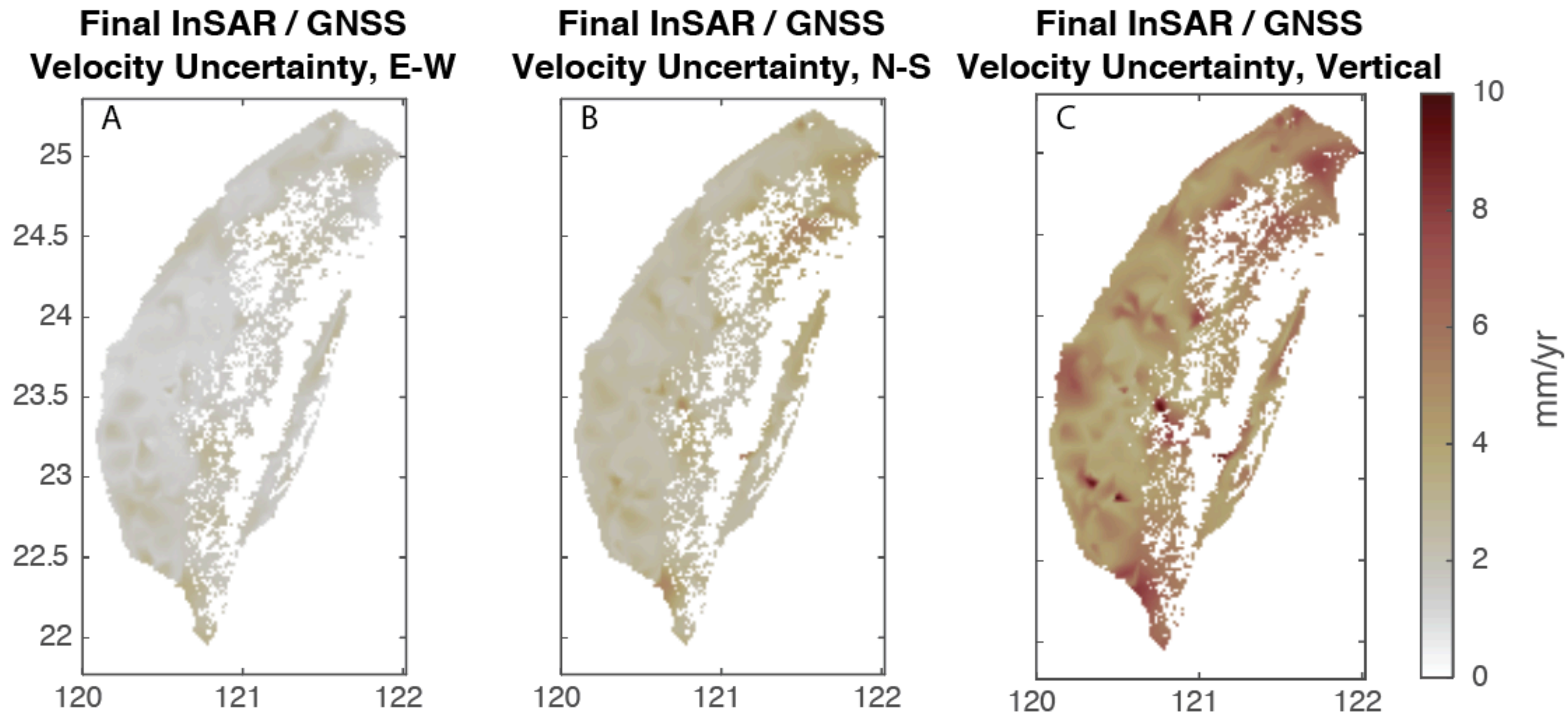

Figure S3. Uncertainty values produced from transforming GNSS-corrected ascending and descending LOS InSAR velocities and interpolated GNSS velocities to the FIG dataset with (A) east-west, (B) north-south, and (C) vertical velocities.

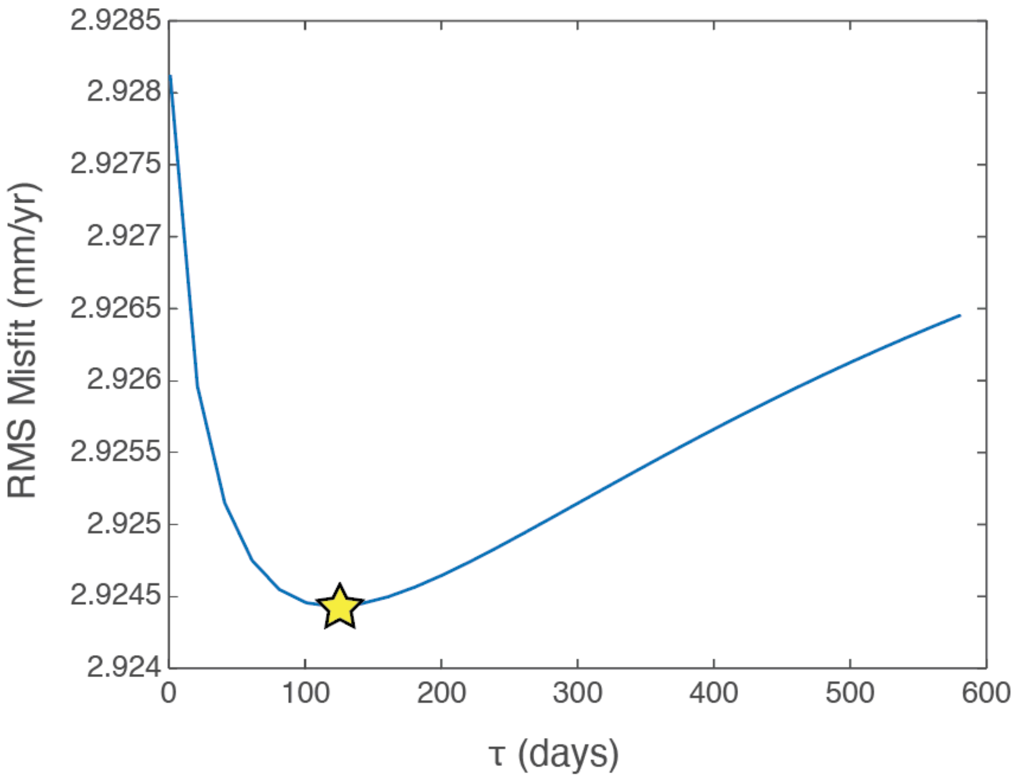

Figure S4. RMS misfits produced from utilizing various τ values (0 to 600 days in 20-day step sizes) in the transformation of observed velocities to modeled velocities. The yellow star indicates τ = 121, which is associated with the lowest RMS misfit estimation.

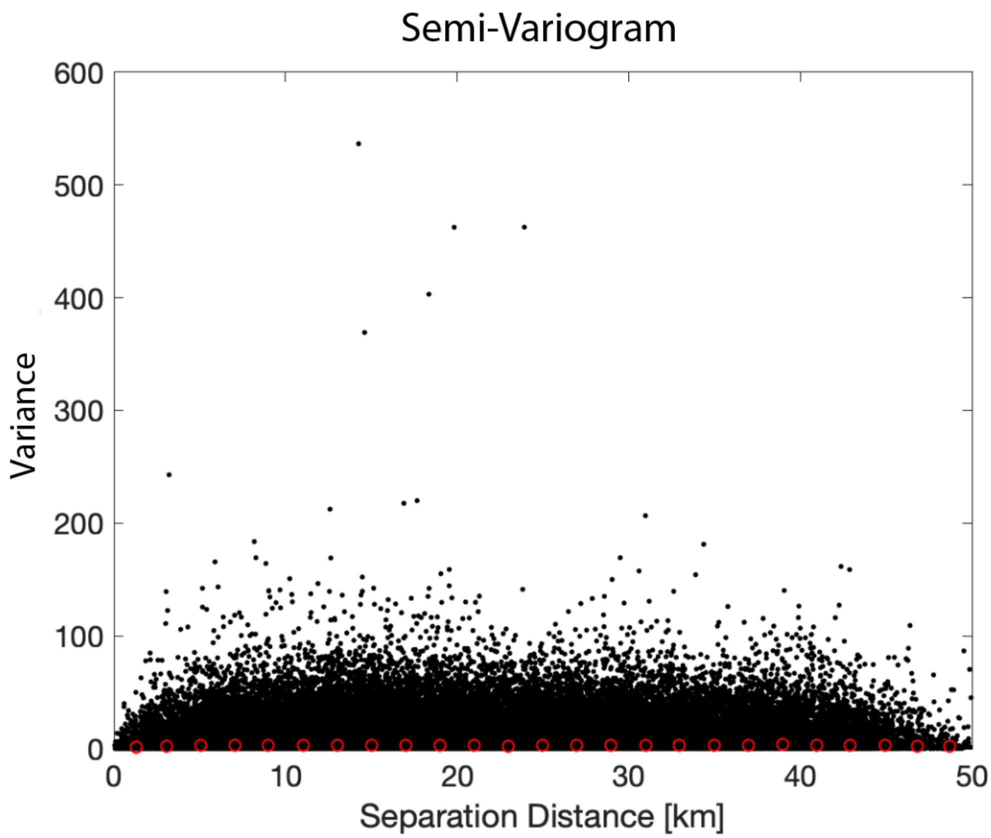

Figure S5. Semi-variogram displaying variance as a function of separation distance for each and all pixels. The open red circles represent the relative locations along the x-axis used for binning the data.

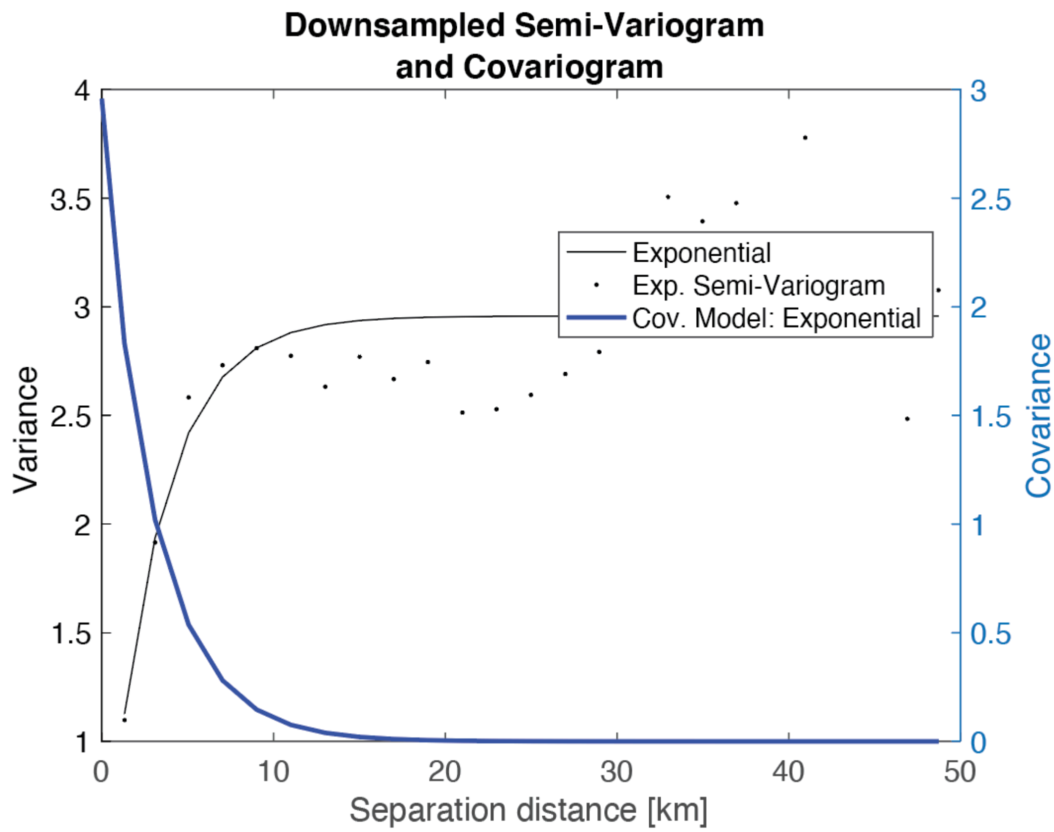

Figure S6. Downsampled semi-variogram displaying variance between each and all pixels as a function of distance. Overlain is the best fit exponential model. Inverted from the semi-variogram is the exponential covariogram model.

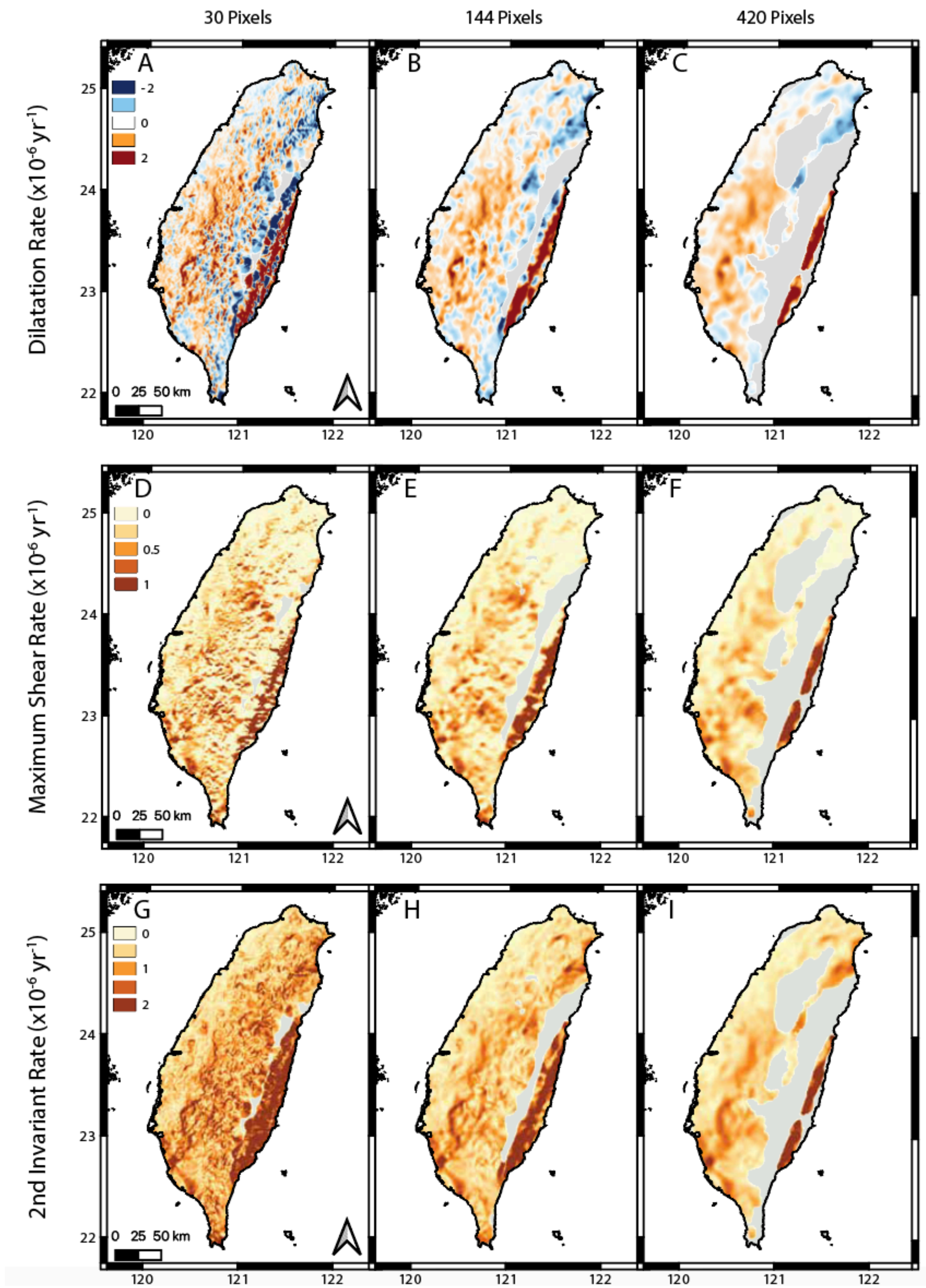

Figure S7. Deformation rate analysis with (A, B, C) dilatation rate, (D, E, F) maximum shear rate, and (G, H, I) 2nd invariant rate in (A, D, G) 30-pixel resolution, (B, E, H)144-pixel resolution, and (C, F, I) 420-pixel resolution. Positive dilatation values indicate contraction and negative values indicate expansion. High maximum shear values indicate increased shearing. 2nd invariant values describe both dilatation and maximum shear as total strain rate accumulation. Gray indicates regions of no data.

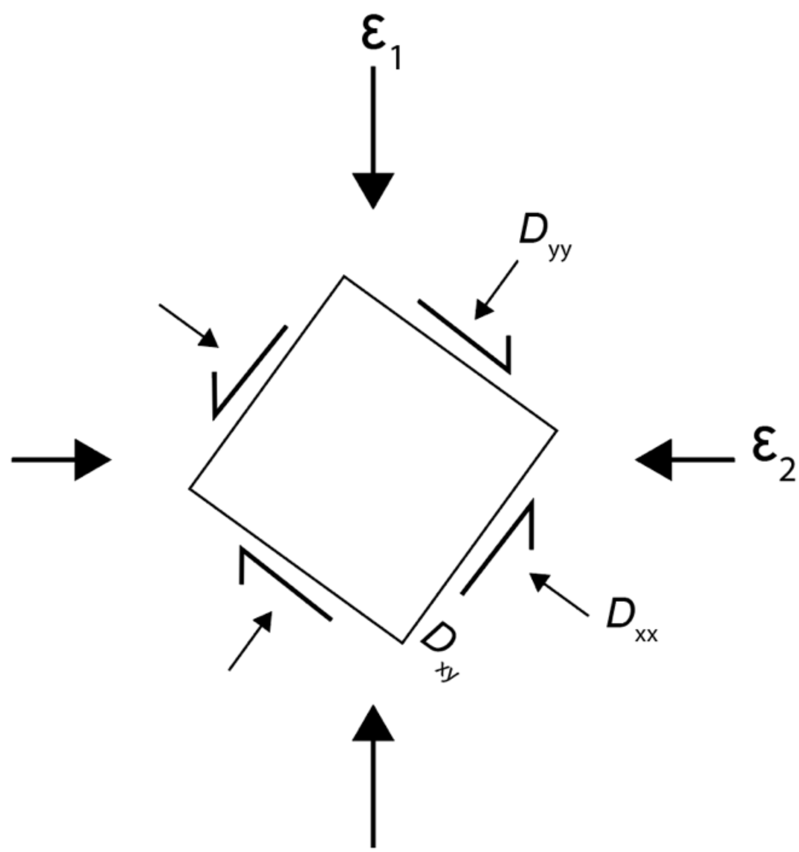

Figure S8. Schematic of maximum (ε_1) and minimum (ε_2) principal strains and the corresponding strain tensor components (D_{xx}, D_{yy}, D_{xy}) influencing a square. This schematic does not consider rotation.

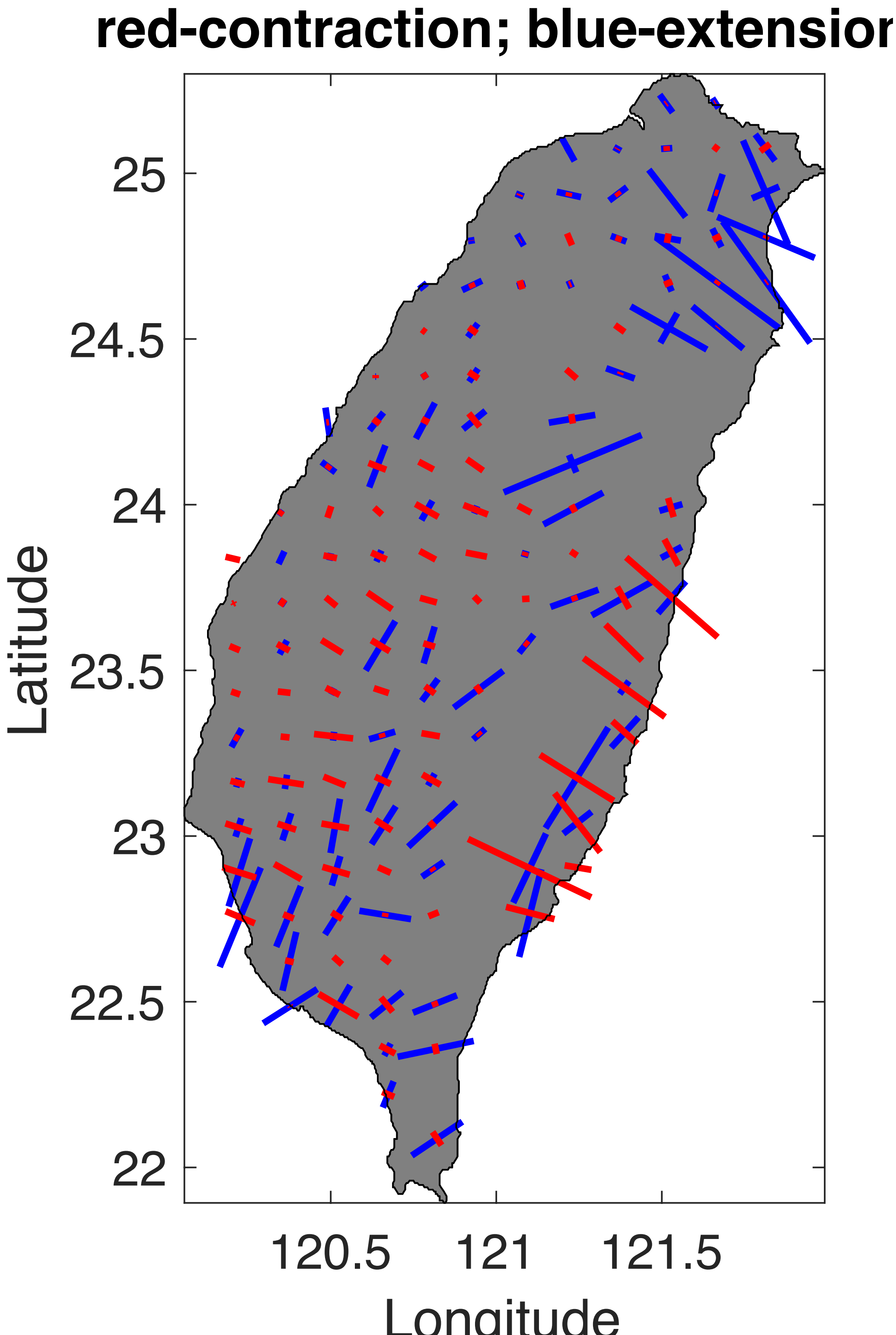

Figure S9. Overview of principal strain rates of Taiwan.

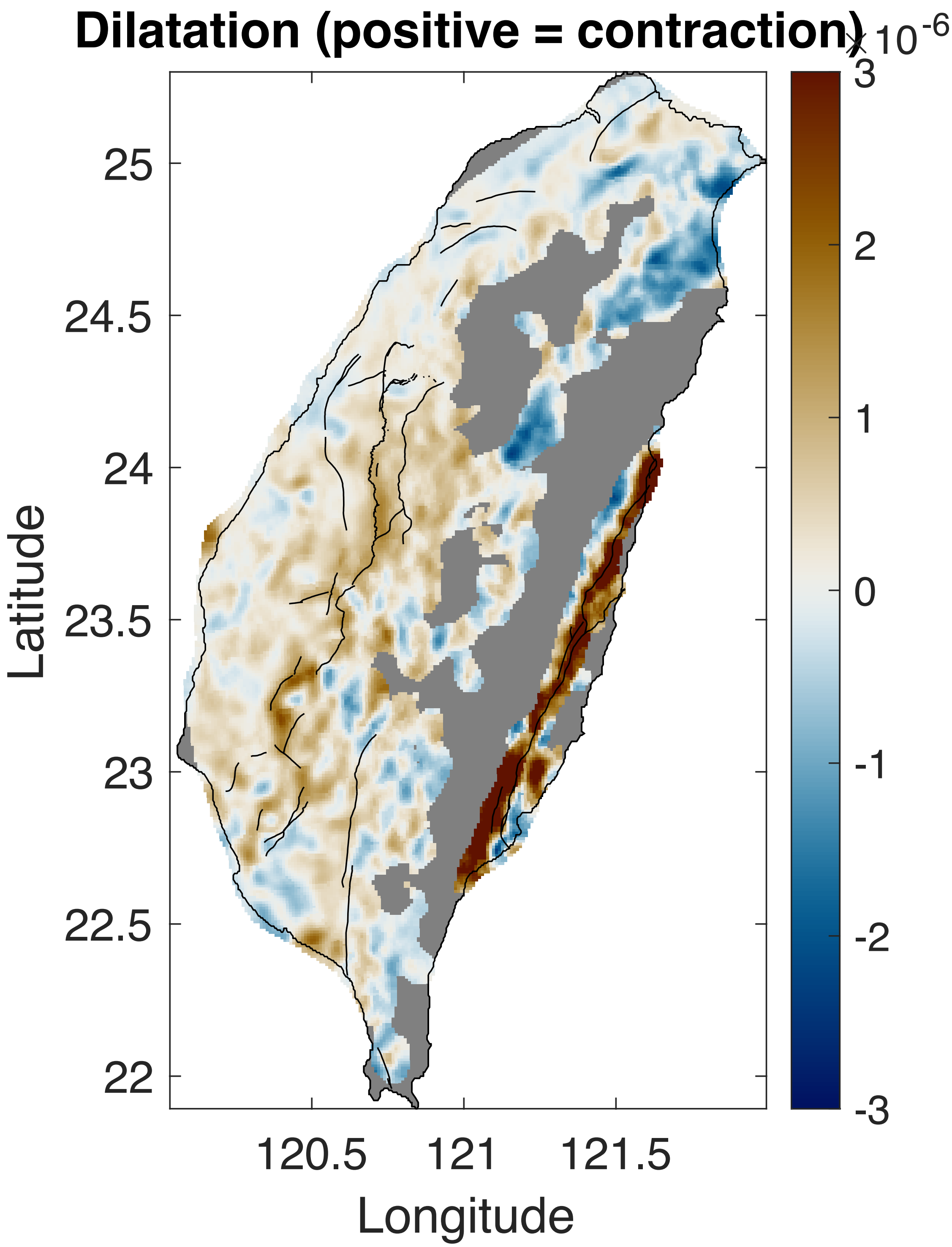

Figure S10. Overview of dilatation rate of Taiwan.

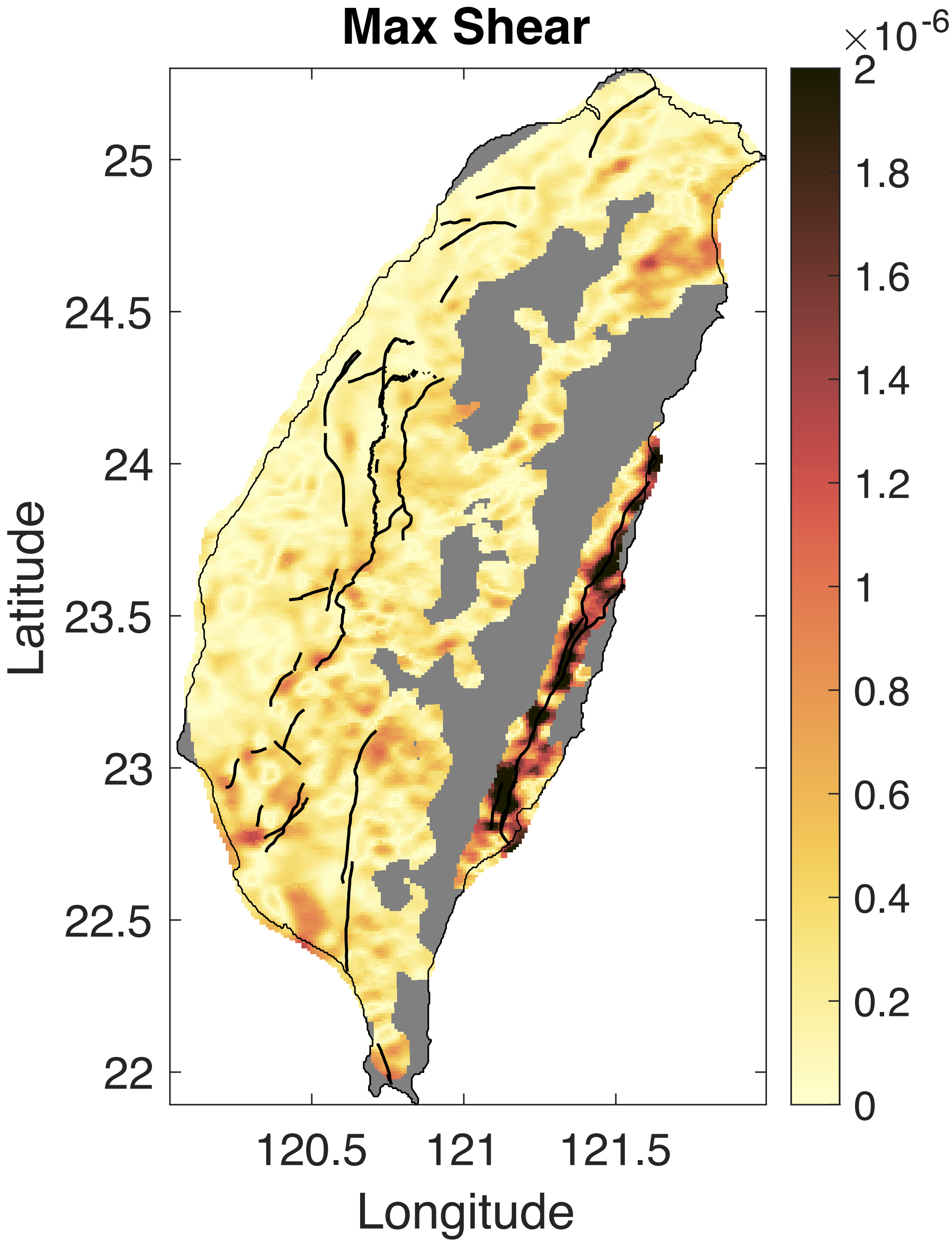

Figure S11. Overview of maximum shear rate of Taiwan.

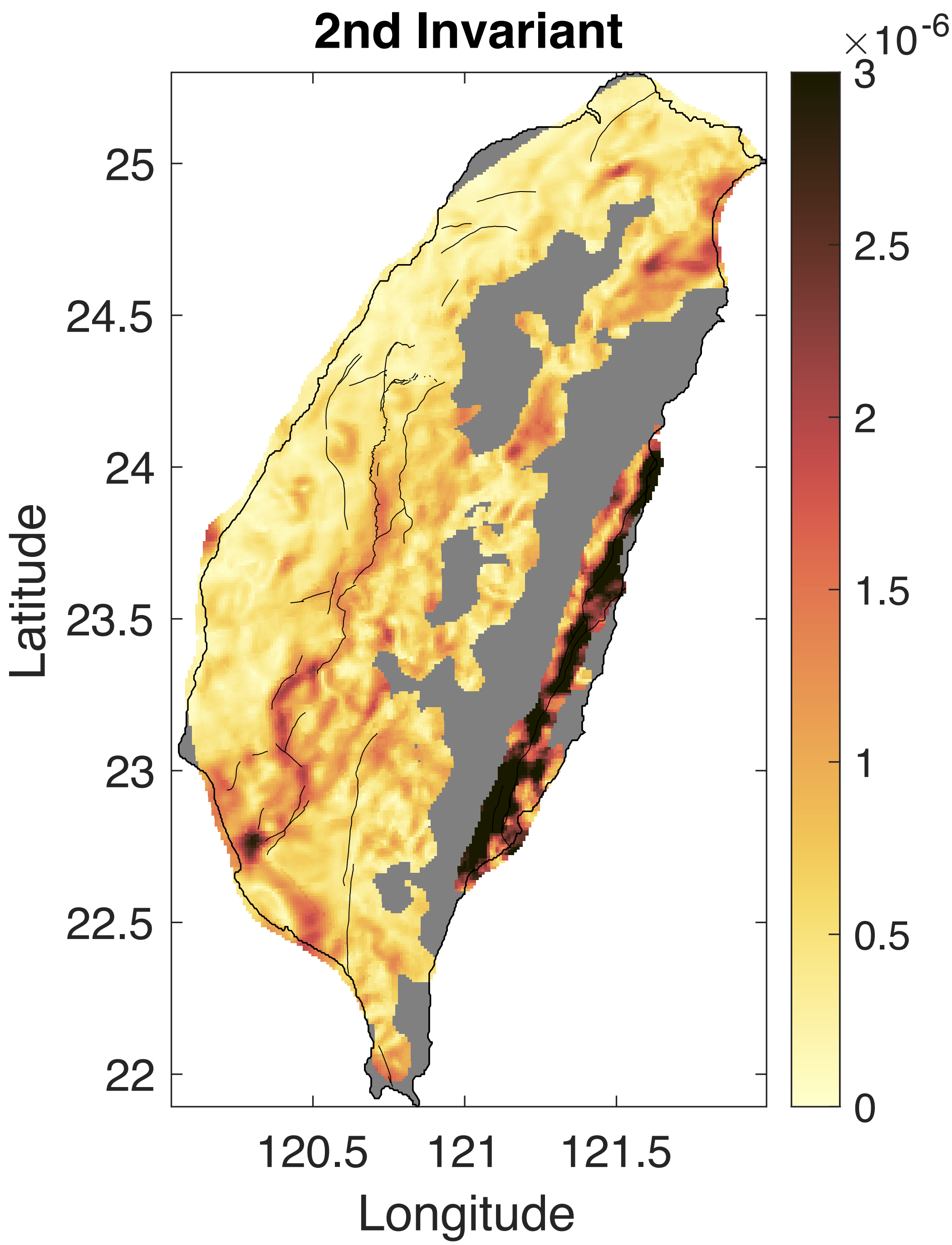

Figure S12. Overview of second invariant of the strain rate tensor of Taiwan.

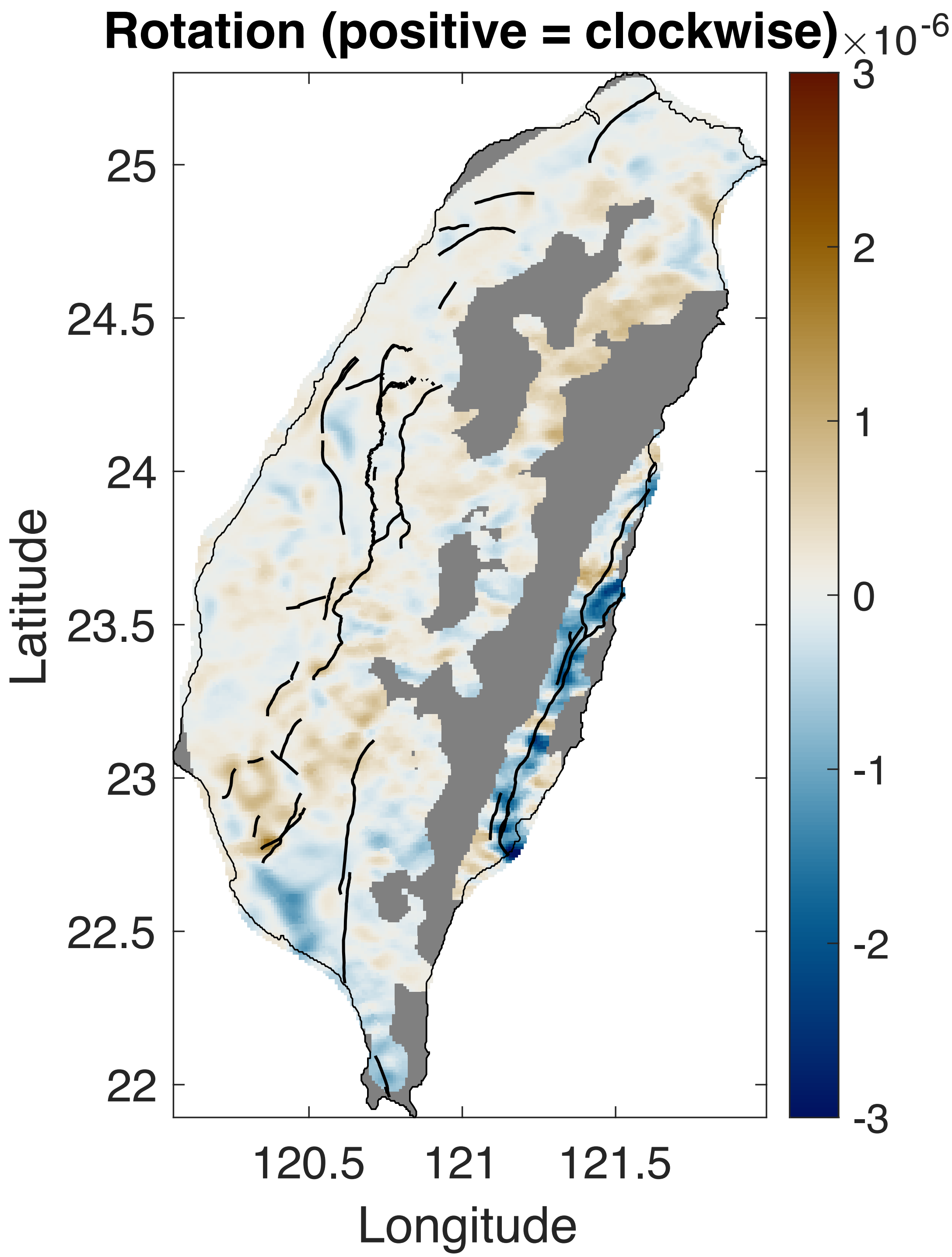

Figure S13. Overview of rotation rate of Taiwan.